Research Square

Preprints are preliminary reports that have not undergone peer review.
They should not be considered conclusive, used to inform clinical practice,
or referenced by the media as validated information.

Glycolytic enzymes play important roles in innate immune memory of neuroimmune responses triggered by systemic inflammation

Raymond Chuen Chung Chang

rccchang@hku.hk

The University of Hong Kong https://orcid.org/0000-0001-8538-7993

Kate Inyoung OH

The University of Hong Kong https://orcid.org/0000-0001-5932-8594

Kornelia Gladysz

The University of Hong Kong

Jung Sun YOO

The Hong Kong Polytechnic University

Gordon Tin Chun Wong

Department of Anaesthesiology, LKS Faculty of Medicine, The University of Hong Kong
https://orcid.org/0000-0002-8127-4593

Article

Keywords: Neuroimmune responses, systemic inflammation, activation of macrophages/microglia, infiltration of macrophages, metabolic changes, trained innate immunity, mitochondrial damage, DNA damage, glycolytic enzymes, metabolic reprogramming

Posted Date: September 23rd, 2026

DOI: https://doi.org/10.21203/rs.3.rs-10771145/v1

License: This work is licensed under a Creative Commons Attribution 4.0 International License.
Read Full License

Additional Declarations: (Not answered)

Title page

Title of manuscript

Glycolytic enzymes play important roles in innate immune memory of neuroimmune responses triggered by systemic inflammation

A running title

Glycolytic enzymes in innate neuroimmune memory

The full name of authors including their given names

Kate Inyoung OH [1,2,3], Kornelia GLADYSZ [4], Jung Sun YOO [3], Gordon Tin Chun WONG [*1], Raymond Chuen Chung CHANG [*2].

The affiliations (including city, state, country and zip code) of all authors

1. Department of Anaesthesiology, School of Clinical Medicine, LKS faculty of Medicine, The University of Hong Kong, Pokfulam, Hong Kong SAR, China, 999077

2. Laboratory of Neurodegenerative Diseases, School of Biomedical Sciences, LKS faculty of Medicine, The University of Hong Kong, Pokfulam, Hong Kong SAR, China, 999077

3. Optical Imaging Group for Translational Medicine, Department of Health Technology and Informatics, The Hong Kong Polytechnic University, Hung Hom, Kowloon, Hong Kong SAR, China, 999077

4. Dana-Farber Cancer Institute, Harvard Medical School, Brookline Ave, Boston, Massachusetts, USA, 02215

The official email addresses

Dr. Kate Inyoung OH, ikateoh@connect.hku.hk

Dr. Kornelia GLADYSZ, kornelia.gladysz@gmail.com

Prof. Jung Sun YOO, jungsun.yoo@polyu.edu.hk

Prof. Gordon Tin Chun WONG, gordon@hku.hk

Prof. Raymond Chuen Chung CHANG, rccchang@hku.hk

The contacts of the corresponding authors

Prof. Gordon Tin Chun WONG, Telephone: +852-9810-8096, Fax number: +852-2255-3303

Prof. Raymond Chuen Chung CHANG, Telephone: +852-9731-8909

Funding

This study was supported by Hong Kong PhD Fellowship Scheme (HKPFS) of National Research Funding (NRF) of Hong Kong and HKU Presidential Scholarship (HKUPS) of The University of Hong Kong (HKU) from Sep 2021 to Aug 2025; funding awarded to Kate Inyoung OH

The study is partially supported by Bingei and L & T Charitable Foundation Professorship in Dementia Research; funding awarded to Prof. Raymond CHANG

Abstract

Neuroimmune responses can be induced by either sterile or non-sterile systemic inflammation. Here, we report that sustained neuroimmune responses in the hippocampus are orchestrated by sequential activation of residential microglia and infiltrating monocytes/macrophages, in which glycolytic shift and mitochondrial damage in microglia play pivotal roles in modulating innate immune memory. Neuroimmune responses are evident from day 2 and persist until at least day 14, well after the systemic inflammation had been resolved. Using day 14 samples for comparison, we found the intensity of responses was more profound after repeated systemic challenges when compared with just one episode, along with increased anxiety behaviors in mice. Microglia mitophagy and hippocampal DNA damage attracted more monocytes/macrophages into the CNS. Concomitantly, glycolysis was enhanced and tricarboxylic acid cycle activity was reduced in the hippocampus. Furthermore, knockdown of phosphofructokinase in microglia by recombinant adeno-associated viruses reduced the mitochondrial and DNA damage and consequently resulted in the resolution of the neuroimmune responses. This study advances our understanding of how metabolic changes and mitochondrial damage may signal the infiltration of monocytes/macrophages into the CNS to sustain the neuroimmune responses after systemic inflammation. In addition, downregulation of enhanced glycolysis may be the therapeutic target to prevent mitochondrial and DNA damage and hence neuroinflammation.

Keywords

Neuroimmune responses, systemic inflammation, activation of macrophages/microglia, infiltration of macrophages, metabolic changes, trained innate immunity, mitochondrial damage, DNA damage, glycolytic enzymes, metabolic reprogramming

Introduction

Immune crosstalk between the periphery and the brain are increasingly recognized for its contribution to neurological and behavioral changes [1-5]. Systemic inflammation can alter the blood-brain barrier (BBB) integrity facilitating the infiltration of peripheral immune cells into the central nervous system (CNS) [2,6,7].

Neuroimmune responses are characterized by the activation of microglia, CNS residence macrophages, that play major roles in innate immune responses in the brain [7-9]. Specific receptors on microglia, e.g. toll-like receptors (TLRs), interleukin-1 receptor type 1 (IL-1R1) and stimulator of interferon genes (STING), are activated by various signals derived from peripheral systems, the infiltrated cells as well as the residence cells triggering the downstream signaling pathways [10-12].

It is often considered as a sign of recovery from the systemic inflammation when the diagnostic levels are back to normal, particularly via the liquid biopsy of the body [13,14]. However, some of the patients display delirium and cognitive decline afterwards [1,15]. Furthermore, the individuals who have experienced long-COVID often complain of deficits in sustained attention and memory [8,16,17]. From these observations, this study aimed to investigate the sustained neuroimmune responses after either sterile or non-sterile systemic inflammation in the hippocampus of mice, which is a key brain structure crucial for learning and memory [18,19].

Recent studies suggested that innate immune cells can be trained to have immune memory, which had long been considered as a unique feature of adaptive immune cells only, e.g. T and B lymphocytes [20-22]. According to the current reports, the trained innate immune memory is characterized by epigenetic modification and metabolic changes in the innate immune cells. Consequently, these changes lead to the alteration of gene expression and enhanced responses of trained innate immune cells [22-25]. In this study, to understand whether the trained innate

immune memory would be beneficial or harmful in the brain, the differential neuroimmune responses and the metabolic changes in the hippocampus of mice were investigated after one or twice of systemic inflammation. In addition, the strategy of therapeutic intervention in the neuroimmune responses were suggested.

Results

Neuroimmune responses induced by sterile systemic inflammation

To demonstrate the presence and persistence of neuroimmune responses in the hippocampus after systemic inflammation, we examined for evidence of microglial activation (Supplementary figure, Fig S1.A and S1.B) and DNA damage (Fig S1.C and S1.D) on post-operative days (PODs) 2, 3 and 14 in hippocampal tissues. The POD 2 hippocampal microglia showed a hyper-ramified morphology representative of functional activation. By POD 14, most of the microglia displayed dystrophic morphology characteristics of cellular senescence and dysfunction [26,27]. The activated Iba1^{+} microglia expressed STING signals (Fig S1.A and S1.B), a crucial part of innate immune defense system that is activated by the abnormal presence of double stranded DNA in the cytosol [12,28]. In addition, the immunoreactivity of gamma-H2AX (γH2AX) was significantly increased in the POD 14 hippocampus (green dots, Fig S1.C and S1.D). Thus, neuroimmune responses are activated by day 2 or 3 after sterile systemic challenge and persisted until at least day 14 when DNA damages in the hippocampus were present.

To investigate whether neuroimmune responses were further modulated after a repeated inflammatory episode, a second systemic challenge was introduced 28 days after the first challenge, allowing sufficient time for recovery between challenges (Fig 1.A). Behavior testing of mice was conducted for three consecutive days prior to tissue harvest on POD 14 after induction of inflammation (Fig 1.B). The locomotor activity of mice was significantly reduced after the second inflammatory episode, and they stayed on the outer edge rather than the center of the arena indicating significantly high anxiety levels. The NOR latency times were significantly increased due to the significantly reduced locomotor activity (Fig 1.B).

The mRNA expression levels of various markers were analyzed to assess the activation levels of macrophages/microglia in the hippocampus (Fig 1.C). The pro-inflammatory markers (STAT1, CD86, IL6) were significantly increased after both single or repeated sterile inflammatory challenges. In addition, anti-inflammatory markers were also significantly increased after the first sterile systemic inflammation (IL-10) and the second systemic episodes (ARG1, CD206, Retnla) (Fig 1.C).

Metabolic changes in the hippocampus after sterile systemic inflammation

To characterize the metabolic changes in the hippocampus after one or two sterile systemic inflammation, the amounts of metabolites (Fig 1.D) and the mRNA expression levels of glycolytic enzymes (Fig 1.E) were analyzed. Overall, the mRNA expression levels of glycolytic enzymes were significantly increased in the hippocampus. Meanwhile, the mRNA expression levels of pyruvate dehydrogenase E1 subunit alpha 1 (Pdha1), which converts pyruvate into acetyl-CoA that feeds into the tricarboxylic acid (TCA) cycle, were significantly decreased. On the other hand, the expression levels of pyruvate dehydrogenase kinase 1 (Pdk1), which suppresses Pdha1, was significantly increased (Fig 1.E and 1.F). Furthermore, the earlier glycolytic metabolites were increased whereas the latter ones such as pyruvate and lactate, as well as TCA cycle related metabolites, were reduced. Together this indicates that after sterile inflammation there was enhanced glycolysis and attenuated TCA cycle activity associated with the neuroimmune responses in the hippocampus (Fig 1.D and 1.F).

Neuroimmune responses induced by non-sterile systemic inflammation

After non-sterile systemic inflammation, the immunoreactivity of STING (magenta or white colored dots) was highly expressed in microglia harvested on post-injection day (PID) 2

and 3 (Fig S2.A). These microglia displayed dystrophic and hypertrophic morphology suggestive of them being in a transitional state actively releasing inflammatory cytokines and phagocytosing [29,30]. The locomotor activity of mice was significantly reduced after the second inflammatory episode and the animal preferentially stayed outer edge of the open arena (Fig 2.B), indicative of significantly higher anxiety levels.

The activated microglia displayed dystrophic morphology after the second non-sterile systemic inflammation. In addition, the immunoreactivity of CD121a (IL-1R1) was increased in the activated microglia (Fig S2.B). There were significant increases in mRNA expression levels of pan-marker of macrophages/microglia (Adgre1, F4/80), as well as pro-inflammatory markers (CD86, CCR2, IFN-γ, STING) and anti-inflammatory markers (ARG1, CD206, IL-10, STAT6, Retnla) after both the first and second challenges. (Fig 2.C).

The isolated cells from the hippocampus were able to separate by the specific markers into microglia (CD11b+CD45low) or macrophage-like cells (CD11b+CD45high) (Fig S2.E). To investigate whether the pro-inflammatory and anti-inflammatory markers were expressed by the microglia and macrophage-like cells, the isolated cells were sorted accordingly and then the mRNA expression levels were analyzed. Indeed, the microglia and macrophage-like cells have expressed significantly increased levels of pro-inflammatory markers (CCR2, TNFα, STAT1, IFN-γ, STING) as well as anti-inflammatory markers (CD206, IL-10, Retnla, STAT6) after both the first or second systemic inflammation (Fig S2.F).

Metabolic changes in the hippocampus after non-sterile systemic inflammation

The amounts of glycolytic metabolites were significantly increased. In addition, succinic acid and malic acid significantly accumulated in the hippocampus, suggestive of the attenuation of TCA cycle in neuroinflammation [31,32] (Fig 2.D and 2.E). The hippocampal

mRNA expression for the enzymes involved in the initiation of glycolysis and PPP, hexokinase 1 (HK1), NADPH oxidase 1 (NOX1) and 6-phosphofructo-2-kinase/fructose-2,6-biphosphatase 2 (Pfkfb2, Pfk2) were significantly increased after one and repeated exposure to LPS. Meanwhile, the other glycolytic enzymes including Pdha1, the gate keeper of TCA cycle, were significantly reduced (Fig 2.F and 2.G), consistent with the change after sterile systemic inflammation.

The microglia sorted from the hippocampus (Fig S2.E) displayed significantly increased mRNA expression levels of glucose-6-phosphate isomerase 1 (Gpi1), Nox1 and Pfkfb2 that facilitate the activation of PPP, after one or repeated challenges (yellow and red bars, Fig S2.I). Meanwhile, after the second challenge, the macrophage-like cells sorted from the hippocampus expressed significantly decreased levels of Pfkfb2 (Fig S2.I) but significantly increased levels of pyruvate kinase (Pklr) (purple bars, Fig S2.I).

The fluorescence intensity of mitoTracker-Red in microglia was significantly decreased after one or repeated inflammatory episodes (Fig S2.G) as was the mitochondrial DNA (mtDNA) copy number. Likewise, the mtDNA copy number was also significantly decreased in the macrophage-like cells after the first but not the repeated episode where it was significantly increased (Fig S2.H).

These data suggested that the metabolic changes were associated with the attenuation of mitochondria in microglia and macrophage-like cells after the first challenge with it becoming more prominent in microglia after the second challenge. On the other hand, the switched metabolic features of macrophage-like cells after the second challenge was accompanied by increasing mtDNA copy number.

Detection of Mitochondrial damage in the hippocampus after sterile or non-sterile systemic inflammation

To determine whether these metabolic changes had implication in mitochondrial damage in microglia, a recombinant adeno-associated virus (rAAV) was designed and adapted to mice via intracerebroventricular (i.c.v) injection to deliver Iba1-mt-mKeima into the microglia. Indeed, the levels of mitophagy (yellow to red) in microglia were significantly increased in the hippocampus after non-sterile (Fig 3.A and 3.C) or sterile systemic inflammation (Fig 3.B and 3.D) as measured by Iba1-mt-mKeima. Notably, the immunoreactivity of lactylation was markedly reduced in the hippocampus after laparotomy (Fig 3.B) and corresponded with the reduced lactate seen in metabolomic analysis (Fig 1.D and 1.F). This contrasts with the Warburg effect seen in pro-inflammatory immune cells or cancer cells [33,34], characterized by increased lactate production and accumulation from enhanced aerobic glycolysis.

In addition, the levels of DNA damage as indicated by γH2AX were also significantly increased in the hippocampus after non-sterile or sterile systemic inflammation, particularly in those microglia with high levels of mitophagy (Fig 3.C and 3.D). These data suggested that the combination of enhanced glycolysis and attenuated TCA cycle are associated with microglial mitochondrial damage and DNA damage in the hippocampus.

The effects of downregulating microglial glycolysis on hippocampal neuroimmune responses after sterile systemic inflammation

To downregulate the enhanced glycolysis in post inflammatory macrophages/microglia, rAAVs were designed and introduced to the mice via intracerebroventricular (i.c.v) injection (Fig 4.A and 4.B). Downregulation of phosphofructokinase 1 (Pfk1) or Pfk2 in microglia

caused significant reduction in the initial glycolytic metabolites, glucose-6-phosphate and fructose-6-phosphate (Fig 4.C and 4.D). In addition, the levels of microglial mitophagy (ratio of MFI-red, Fig 4.E, 4.F and 4.H) as well as hippocampal DNA damage (magenta, Fig 4.E, 4.F and 4.J) were significantly reduced after downregulation of microglial Pfk1 or Pfk2 after sterile systemic inflammation.

The immunoreactivity of γH2AX among the immune cells and the number of cells were significantly decreased by the downregulation of microglial Pfk1 or Pfk2 after sterile systemic inflammation (Fig 4.L and 4.M). Notably, the immunoreactivity of histone lactylation and the number of cells among the isolated immune cells were significantly increased by downregulation of microglia Pfk1 after the first sterile systemic inflammation (Fig 4.N and 4.O).

Effects of downregulation of microglial glycolytic enzymes on the innate immune reactions in the hippocampus after sterile systemic inflammation

The immunoreactivity of activated microglia (anti-Iba1) was significantly increased in the hippocampus after laparotomy (Fig 5.C). On the other hand, the immunoreactivity of homeostatic microglia (anti-P2RY12) was significantly decreased in the hippocampus of the mice (Fig 5.E).

Meanwhile, the immunoreactivities were changed by downregulating microglial glycolytic enzymes. Both activated microglial (Fig 5.D) and homeostatic microglial immunoreactivities (Fig 5.F) were increased, particularly by downregulating microglial Pfk1 after the first sterile systemic inflammation (The left, Fig 5.D and 5.F). The immunoreactivities were decreased upon the downregulation of the enzymes after the second systemic inflammation (The right, Fig 5.D and 5.F).

196 The flow cytometry analysis illustrated consistent results with the data of IHC described
197 above on the innate immune reactions. Downregulation of microglial Pfk1 led to significantly
198 increased number of macrophage-like cells ($CD11b^{+}CD45^{high}$) in the hippocampus after the
199 first sterile systemic inflammation (the left, Fig 5.G and 5.H). On the contrary, downregulation
200 of the enzymes caused significantly decreased MFI and number of macrophage-like cells after
201 the second sterile inflammation consistently (the right, Fig 5.G and 5.H).

202 Furthermore, the population of STING immunoreactive cells among the immune cells
203 dramatically increased but the MFI of the cells were significantly decreased by downregulating
204 microglial Pfk1 after the first sterile systemic inflammation (the left, Fig 5.I and 5.J). The
205 immunoreactivity of IL-1R1 (CD121a) and the number of cells were significantly decreased
206 by downregulation of the enzymes after the first challenge (the left, Fig 5.K and 5.L). Notably,
207 the immunoreactivity of IL-1R1 and the number of cells among the isolated immune cells were
208 dramatically increased after the second sterile systemic inflammation even after the
209 downregulation of microglial Pfk1. Interestingly, the immunoreactivity of IL-1R1 was
210 significantly decreased by downregulation of microglial Pfk2 after the second sterile systemic
211 inflammation (the right, Fig 5.K and 5.L).

212

213 **The effects of downregulating microglial on the neuroimmune responses after non-sterile**
214 **systemic inflammation**

215 In the hippocampus of negative control (NC) mice, downregulation of microglial Pfk1
216 caused significantly increased amounts of alpha-ketoglutaric acid (AKG), an observation that
217 is considered to confer anti-inflammatory and anti-aging benefits [35,36]. There were no
218 significant changes in the amounts of hippocampal glycolytic metabolites after non-sterile
219 systemic inflammation in mice with downregulated microglial Pfk1 or Pfk2 (Fig 6.B and 6.C).

However, it led to dramatically reduced levels of microglial mitophagy and DNA damage in the hippocampus.

The levels of microglial mitophagy in the hippocampus were significantly increased after non-sterile systemic inflammation (Fig 6.F). The microglial mitophagy was significantly decreased by downregulation of microglial glycolytic enzymes after LPS challenges (Fig 6.G). In addition, the immunoreactivity of γH2AX was dramatically increased after non-sterile systemic inflammation (Fig 6.H). Alteration of the microglial glycolytic enzymes led to significant reduction of the DNA damage in the hippocampus (Fig 6.I).

The MFI of γH2AX immunoreactivity among the immune cells was significantly decreased after downregulation of microglial Pfk1 despite an increased number of cells (Fig 6.J and 6.K). Furthermore, consistent with the changes in the hippocampus after sterile challenge (Fig 4.N and 4.O), downregulation of microglial glycolytic enzymes significantly increased the population of histone lactylated immune cells after non-sterile challenge (Fig 6.L and 6.M).

Effects of downregulation of microglial glycolytic enzymes on the innate immune reactions in the hippocampus after non-sterile systemic inflammation

The immunoreactivity of the activated microglia (Iba1+) was significantly increased in the hippocampus after the first non-sterile systemic inflammation (The orange plot, Fig 7.C). Meanwhile, it was significantly decreased after the second non-sterile systemic inflammation (The red plot, Fig 7.C). The levels of homeostatic microglia (P2RY12) in the hippocampus were dramatically decreased after the first and second LPS challenges (Fig 7.E). Meanwhile, downregulation of phosphofructokinases in microglia led to significantly increased

immunoreactivities of the activated microglia (Fig 7.A, 7.B and 7.D). It also significantly enhanced the immunoreactivity of homeostatic microglia in the hippocampus (Fig 7.F).

There was significantly increased population of microglia ($CD11b^{+}CD45^{low}$) in the hippocampus by downregulation of microglial glycolytic enzymes but reduced population of macrophage-like cells ($CD11b^{+}CD45^{high}$) in the hippocampus (Fig 7.G and 7.H). In addition, the immunoreactivity of STING of the immune cells and the number of cells in the hippocampus were significantly increased by downregulating the enzymes (Fig 7.I and 7.J). Meanwhile, the immunoreactivity of IL-1R1 (CD121a) was significantly decreased in the hippocampus, although the number of cells significantly increased (Fig 7.K and 7.L).

Discussion

The chief findings from this study demonstrated that a central neuroimmune response can be sustained in the hippocampus beyond the resolution of the initiating inflammatory response. A second inflammatory challenge can result in an exaggerated neuroimmune responses as characterized by the presence of more prominent dystrophic microglia (S 2.B) as well as highly enhanced immunoreactivity of STING entire the brain (S 2.C), suggesting that microglia be primed to have trained innate immune memory causing sustained neuroimmune responses [37,38]. This result in microglia is being more responsive against subsequent challenges but it remains unclear whether this trained innate immune memory is more likely beneficial or harmful in disease progression [39,40]. Further we demonstrated that there was enhanced glycolysis and attenuated TCA cycle activity associated with the neuroimmune responses following sterile inflammation with associated microglial mitochondrial and DNA damage.

The activated hippocampal microglia from the post-inflammatory mice displayed increased immunoreactivity to STING and CD121a (IL-1R1). This positive feedback loop of STING and

CD121a was possibly triggered by the cytosolic dsDNA including mtDNA and nDNA. Activated STING and excessive NO can facilitate the secretion of IL-1β, which plays a critical role in the metabolic change by enhancing glycolysis and stabilizing HIF-1α [41,42]. Stabilized HIF-α promotes the related genes including Pdk1 [43,44], which was significantly increased after systemic inflammation (Fig 1.E and 1.F). Indeed, the metabolic changes after systemic inflammation were abundant in the hippocampus, which were characterized by enhanced glycolysis and attenuated TCA cycles. These metabolic changes became more prominent after the second challenge (Fig 1.D and 1.F).

The amount of succinate was significantly increased after systemic inflammation (Fig 2.D, 2.E and 2.G). Accumulation of succinate can be implicated in metabolic disorders and neurodegenerative diseases. Its accumulation can induce epigenetic modifications via succinylation, a post translational modification characterized by the addition of a succinyl group to a lysine residue on a protein that in turn can significantly change the structure and functions of protein. Succinylation can change the charge of the lysine residue from positive to negative that potentially impacts protein folding, stability and interaction with other molecules. In addition, succinyl group is larger (100 Da) than other modifications such as methylation (14 Da) and acetylation (42 Da), this increase in size can lead to significant structural changes [45-47]. Succinylation is basically involved in mitochondrial metabolism. Upon mitochondrial damage, accumulated succinate can lead to succinylation of amyloid precursor protein (APP) and tau that promote the accumulation of Aβ and tau aggregation, respectively [48-51]. In addition, studies suggested that upregulated succinylation can induce senescence in microglia upon the alteration of mitochondrial metabolism [46].

There were significantly increased number of the activated macrophages/microglia (Iba1+) detected in the choroid plexus, which is the border area between the hippocampus and ventricles (S 2.D). The isolated microglia and macrophage-like cells after one systemic

challenge displayed significantly decreased levels of mtDNA copy number. After a repeated challenge, the microglia expressed dramatically reduced levels of mtDNA copy numbers, indicating that there might be mitochondrial dysfunction. In contrast, macrophage-like cells in the hippocampus, possibly of peripheral origins, displayed significantly increased levels of mtDNA copy number after the second challenge (Fig 2.G and 2.H). These data suggest that the observed metabolic changes may be triggered by mitochondrial dysfunction in the trained microglia as well as the infiltrated cells with the imbalanced metabolic alteration.

The hippocampus displayed significantly increased levels of mitophagy in microglia and DNA damage in the hippocampus (Fig 3, 4 and 6). Enhanced mitophagy, in healthy brains, can help with the removal of damaged mitochondria to prevent further damage [52,53]. Most cells contain hundreds to thousands of mitochondria to buffer against, to some extent, the adverse effects from mitochondrial dysfunction. However, under disease states with impaired homeostasis, mitochondrial damage overwhelms this buffer and result in decreased energy production and excessive oxidative stress that in turn triggers a cascade of events leading to additional neuronal damage [54,55]. Furthermore, mitochondrial damage causes the release of mitochondrial proteins including endonuclease G (EndoG) into the nucleus leading to the DNA damage response. EndoG induces DNA fragmentation including double-strand breaks (DSBs) by activating apoptosis as well as autophagy [56,57] (Fig 8). Thus, this study suggests that the metabolic changes in trained immunity are either caused by or resulted in impaired mitochondrial function that led to further oxidative stress, DNA and neuronal damage.

The next aim of this study was to evaluate whether mitochondrial damage could be decreased by metabolic reprogramming. The key rate-limiting glycolytic enzymes were targeted in microglia to downregulate the enhanced glycolysis in the hippocampus using designed rAAVs (Fig 4.A). Downregulation of microglial Pfk1 by rAAV-Iba1-shPfk1 resulted in reduced microglial mitophagy as well as significantly diminished DNA damage in the

hippocampus (Fig 4 and 6). Furthermore, the body weight after rAAV-Iba1-shPfk1 significantly recovered and increased after systemic inflammation (S 4.A and 4.B). These data suggest that some extent of reduction in glycolysis potentially help to rescue mitochondria and nuclear DNA from persistent neuroinflammation.

Downregulation of microglial Pfk2 by rAAV-Iba1-shPfk2 displayed beneficial effects after the second systemic inflammation. However, it did not improve the condition in the hippocampus (Fig 4 to 8). Pfk2 (also known as Pfkfb2) is a bifunctional glycolytic enzyme that can also regulate Pfk1 activation. Pfk2 catalyzes F-6-P to fructose-2,6-bisphosphate (F-2,6-BP). Conversely, Pfk2 can also convert F-2,6-BP back to F-6-P, which feeds glycolysis [58,59]. This study showed that downregulation of microglial Pfk2 reduced the number of immunoreactive microglia in the hippocampus. In turn, the hippocampus displayed the increased levels of mitochondrial damage in microglia and DNA damage in the hippocampus (Figs 4 to 8). Furthermore, the recovery of body weight after rAAV-Iba1-shPfk2 was significantly slower than those of vehicle or Iba1-shPfk1 (S 4.A and 4.B). These data suggest that the extensive suppression of glycolytic enzymes might be harmful for microglial viability.

Lactate is a byproduct of glycolysis, which is increased upon enhanced glycolysis, for instance after resistant exercise. Other studies reported that increased production of lactate and its accumulation are hallmarks of enhanced aerobic glycolysis, known as the Warburg effect in pro-inflammatory immune cells or cancer cells [33,34]. In this study, meanwhile, the lactate levels in the hippocampus were not significantly increased upon the metabolic changes (Fig 1 and 2). The lactate was possibly taken by neurons for actively utilizing it in energy production as well as cell signaling [60,61]. Indeed, this study illustrated that lactylation, H4K12la, immunoreactivity levels were abundantly high in neurons compared to other CNS cells. Lactylation has been recently suggested to be involved in the formation and sustaining of immune memory. The underlying mechanism and the effect of lactylation on different sites are still undetermined.

342 Considerable controversy questions whether the increased levels of H4K12la is beneficial or
343 harmful [62-66]. Meanwhile, some of the recent studies reported that the enhanced levels of
344 H4K12la in microglia, particularly enriched in the promoter region of Spp1 (encodes the
345 protein, osteopontin), could improve the recovery of spinal cord injury [67].

346 Other researchers reported that lactate derived from resistant exercise has increased the α-
347 secretase activity of a disintegrin and metalloprotease domain-containing protein 10
348 (ADAM10), which cleaves amyloid precursor protein (APP) into non-amyloidogenic manner
349 which helps to prevent the formation of Aβ. On the other hand, lactate could inhibit activity of
350 the β-secretase, beta-site APP cleaving enzyme 1 (BACE1), which cleaves APP to produce Aβ
351 peptides leading to Aβ aggregation and the plaque formation. In turn, the lactate could help to
352 prevent formation of Aβ in the brain, suggesting that lactate plays a critical role in regulating
353 APP processing [68].

354 Notably, in this study, the downregulation of Pfk1 in microglia increased the levels of
355 lactylation, H4K12la, in microglia. This data suggests that the increased levels of lactylation
356 in microglia probably help to reduce mitochondrial and DNA damage. However, further
357 investigation is required into whether there is a direct role of lactylation in reducing the damage.
358 Nonetheless, it was clear that the downregulation of Pfk1 in microglia reduced the
359 mitochondrial and DNA damage, and increased the levels of lactylation in microglia,
360 respectively.

361 This study advanced our knowledge by showing that the neuroimmune responses induced
362 by systemic inflammation can persist over time by the sustained metabolic changes. These
363 findings suggest that moderate downregulation of enhanced glycolysis in microglia can help to
364 prevent neuronal damage in the hippocampus by improving mitochondrial homeostasis. This

might be a promising therapeutic intervention to prevent the neuronal damage induced by systemic inflammation.

Materials and methods

Ethics approval of animal study

Mice housed under an AAALAC International (Association for Assessment and Accreditation of Laboratory Animal Care) accredited program at the Centre for Comparative Medicine Research, HKU under Specific Pathogen Free (SPF) conditions. The animal licenses were approved for conducting experiments with live animals upon section 7 of animals (Control of Experiments) ordinance (Cap. 340) via the Department of Health in Hong Kong, the animal license numbers of [(22-643) in DH/HT&A/8/2/3 Pt.44] and [(23-1029) in DH/HT&A/8/2/3 Pt.63]. The protocols for conducting experiments with live animals were authorized by Committee on the Use of Live Animals in Teaching and Research (CULATR) from the Center for Comparative Medicine Research (CCMR) of The University of Hong Kong (HKU), the CULATR numbers of [22-148] and [24-168].

Animals

C57BL/6J, 4-6 months old, male mice were obtained from the CCMR of HKU. Three to five mice per one cage were housed and kept under a standard housing condition of 12-hour light (7 am to 7 pm) / 12-hour dark cycle maintaining a temperature range of 16 to 26℃, and a humidity controlled within a range of 30-70%. The surgery, injection, behavior tests and body weight records started at 7 am for consistent data.

Laparotomy under sevoflurane

To induce sterile systemic inflammation, laparotomy was operated on the mice. The mice were placed in the inhalation anesthetic chamber connected to vaporizer and ventilator

(RWD Life Sciences, Shenzhen, China), with 2-3% of sevoflurane (Sevorane™, Abbott, Switserland) plus medical oxygen. The mice, with unconscious and no respond to stimuli, were directly replaced on the surgical pad with covering the nose and mouth by the anesthetic mask connected to the same ventilator to anesthesia system.

The procedure of laparotomy was developed from previous research in my current laboratory [1,69]. The hairs on the abdomen were shaved by hair remover cream. All the surgical tools including cotton buds and cotton gauze were pre-sterilized by autoclave for the aseptic operations. The longitudinal midline incision, 1 to 1.5 cm, was made on the abdomen. A part of intestine, 4 to 5 cm, was gently exteriorized using blunt tip forceps and then gently rubbed using sterilized cotton gauze for 30 seconds. The intestine was returned to the abdominal cavity carefully. The muscle layer of abdominal skin was sutured using an absorbable surgical suture (4-0, Vicryl, Ethicon®, USA). The outer skin layer was sutured using a non-absorbable surgical suture (4-0, Ethilon™, Ethicon®, USA). The surgical area was disinfected with 70% alcohol before the operation, and povidone-iodine after the suture. The whole procedures of laparotomy were taken 15 to 20 minutes per mouse. The mice returned to the home cages with fresh bedding kept in the intensive care unit (ICU) at LAU overnight. Then, the mice were housed at the standard condition of LAU until the next experiments either animal behavior tests or euthanasia for further investigations.

Bacterial endotoxin challenges

To induce non-sterile systemic inflammation, the mice were challenged with lipopolysaccharides (LPS, L4130, Sigma-Aldrich, USA) intraperitoneally (i.p). The mice of NC group were injected with normal saline (0.9% sodium chloride), i.p. The mice of LPS group were injected with 100 µl (i.p) of LPS solution (0.1 mg/ml, in saline), respectively, which is

equivalent to 10 μg of LPS per mouse. The initial body weight and end point body weight were recorded, respectively.

Open field tests

To evaluate the general locomotor activities and anxiety levels of the mice, open field tests were conducted. The mice were habituated in dark animal behavior room with an indirect dim light, yellow LED light, for 30 minutes. All the animal behavior tests were conducted in dark with an indirect dim light. Each mouse was placed in the open arena, a square with dimensions of 50 x 50 cm. The activities and movements for the first 10 minutes were recorded and analyzed via the video tracking system, SMART 3.0 (Panlab, Harvard Apparatus, USA). The open arena was virtually gridded into 25 squares (5 x 5) for analysis. In case the anxiety level is high, the animals tend to stay at the outer edge (16 squares) of the arena rather than the center (9 squares) of the arena. The locomotor activities were measured by NIR (near infrared) count and the global activities, respectively.

Immunohistochemistry

To investigate the immunoreactivity of the specific markers in the hippocampus, immunohistochemistry was performed. The mice were anesthetized by intraperitoneally administrating the overdose of Ketamine and Xylazine cocktail (KX, 100 mg/kg of Ketamine + 10 mg/kg of Xylazine). And then the mice were euthanized by exsanguination for collecting whole blood via cardiac puncture.

The whole brain was isolated from the skull for further tissue processing. The brain tissue was fixed in 4% PFA (paraformaldehyde, ChemCruz, Santa Cruz biotechnology, USA) for more than 24 hours. Then, the brain tissue was serially dehydrated by 15% sucrose for at least six hours and by 30% sucrose for more than 24 hours. The brain tissues were coronal

sectioned using vibratome (VT1000S, Leica, Germany) to produce thin slices in 100 micrometers thick. The sections were kept in normal saline containing 0.02% sodium azide (NaN_3) at 4℃ until the antibody staining.

For the antibody staining, the brain tissues were blocked by incubating with 1% BSA (bovine serum albumin, Merck, Germany) on the gentle agitation shaker (60 to 70 rpm) for two hours to prevent non-specific antibody binding. After the blocking, the tissues were washed and permeabilized with 0.3% Triton X-100 (Merck, Germany) for 20 minutes per time, three times on the shaker. The brain sections stained with the specific target primary antibodies, which were diluted in one to one thousand ratio (1:1000) in 1% BSA containing 0.3% Triton X-100 for overnight at 4℃. The primary antibodies were washed out from the sections by 0.3% Triton X-100 (20 minutes, three times). And then, the secondary antibodies conjugated with fluorescence dyes (1:1000 in 1% BSA + 0.3% Trion X-100) were stained to the sections accordingly for three hours at room temperature on the shaker covered by aluminum foil to avoid light exposure. From this step, all the procedures were performed in a dark environment to avoid light, particularly UV (ultraviolet) and blue light. It is to prevent photobleaching, which permanently loss of fluorescence signals. The stained sections were washed with 0.3% Triton X-100 for 20 minutes per time, twice, and then washed lastly with normal saline for 20 minutes. Three sections from different mice were placed in line on one glass slide and mounted with 90% glycerol, pH 9.0, and a wide cover glass was carefully applied avoiding formation of bubbles. The fluorescent images were taken under either LSM 780/800/900 confocal laser scanning microscope (Zeiss, Germany) or Ti2-E widefield fluorescence microscope (Nikon, Japan). The images were opened and extracted via either Zen blue/black (Zeiss, Germany) or Imaris software (Oxford Instruments, Switzerland and USA).

Flow cytometry

To evaluate the specific immunoreactivities of the single cells in the hippocampus, flow cytometry was demonstrated. The mice were euthanized by injecting overdose of KX and performing cardiac puncture as described above. The circulatory system was perfused with 30 ml of normal saline through the left ventricle. The whole hippocampus was isolated from the brain and directly transferred to the normal saline. The hippocampus was homogenized using sterilized medical rubber plungers, which were isolated from 3 ml syringes. The homogenization was performed through 40 μm (micrometer) cell strainer (SPL life sciences, South Korea) placed onto 50 ml conical tube for collecting the isolated single cells in normal saline. The isolated cells were washed with normal saline by centrifugation (700 g force, RCF for 15 minutes). The washed cells were directly fixed by adding 2% PFA for 10 minutes, and then permeabilized by incubating with 0.1% Triton X-100 for 30 minutes. The cells were rinsed with 0.5 % of BSA and then 0.1% of BSA by centrifugation. The rinsed cells were stained with specific antibodies accordingly.

The cells were stained with either primary antibodies without fluorescence conjugation (1:1000 diluted in 0.1% BSA) or antibodies conjugated with specific fluorescence (1:200 diluted in 0.1% BSA) overnight. The primary antibodies were washed out from the cells by adding 0.1% BSA and centrifugation. The primary stained cells without fluorescence were further stained with the specific secondary antibodies conjugated with fluorescence accordingly. The cells were washed by adding 0.1% BSA and centrifugation. All the stained cells were resuspended in 0.1% BSA. The stained single cells were filtered through 40 μm cell strainer just before performing flow cytometry. The cells were confirmed by observing via confocal microscopy.

The filtered cells were applied for analysis and sorting to the flow cytometry instruments, BD FACSAria^{TM} SORP or FACSAria^{TM} Fusion (Becton and Dickinson Biosciences, USA). The nozzle size was set as 100 μm. The voltages of forward scatter (FSC) and side scatter (SSC) were adjusted, and the first gating was set according to the cell size (FSC) and granularity/or internal complexity (SSC) to exclude cell debris or cell clumps. The internal complexity is influenced by the presence of granules, nuclei, or other cellular structures. The second and third gating, linear box, were created in the plotting FSC-A against FSC-H (or FSC-W) and then SSC-A against SSC-H (or SSC-A), respectively. These steps were for separating doublets to distinguish single cells for further analysis.

To verify the specificity of immunoreactive markers of macrophages and microglia, specific markers were tested by stained peritoneal immune cells as a positive control. After this step, anti-CD11b-APC/Cy6 and anti-CD45-BV650 were used to isolate macrophages and microglia.

The voltage of each laser power and gating strategies were adjusted based on the autofluorescence intensities of the isotype control (single cells stained with IgG), respectively. The stained single cells were analyzed and sorted based on the gating strategies. The data was opened and further analyzed by using Flowzo software (Becton and Dickinson, USA).

For the sorting, the cells were stained with anti-CD11b-APC/Cy7 and anti-CD45-BV650. The sorted cells, microglia ($CD11b^{+}CD45^{low}$) and macrophage-like cells ($CD11b^{+}CD45^{high}$), were collected into the sort collection chamber for further experiments. The sorted cells were washed by centrifugation. The first batch of the sorted cells were confirmed by observing under the confocal microscopy. The sorted cells were resuspended in Trizol (RNAiso Plus, Takara, Japan) for RNA extraction or TE (Tris-EDTA, ethylenediamine

tetraacetic acid, Thermo Scientific™, USA) buffer for DNA extraction, depending on the further experiments and stored at freezer.

RNA extraction and cDNA synthesis for qRT-PCR

Total RNA was extracted from either the hippocampus or the sorted cells treated with Trizol in freezer. The samples treated with Trizol were taken out from the freezer and incubated at room temperature for five minutes to permit the complete dissociation of nucleoprotein complexes. Added 200 µl of chloroform per 1 ml Trizol reagent. Capped sample tubes securely and shook the tubes vigorously by hand for 15 seconds and incubated them at room temperature for three minutes. Centrifuged the samples at 14,000 rpm for 15 minutes at 4°C. Transferred carefully the colorless upper aqueous phase to a fresh tube. Added 500 µl of isopropyl alcohol per tube and mix. Incubate samples at room temperature for 10 minutes. Centrifuged at 14,000 rpm for 10 minutes at 4°C. Remove supernatant, added 1 ml of 70% ethanol and mix the sample by vortexing and centrifuge at 14,000 rpm for 10 minutes at 4°C. Removed supernatant, dried roughly the RNA pellet (air-dry) for five to ten minutes. It is important not to let the RNA pellet dry completely as this will greatly decrease its solubility. Dissolved RNA in 50 µl of RNase-free water (DEPC treated water) by passing a few times of pipetting. Incubated for 10 minutes at 55°C. Measured RNA amounts and purity and store at -80°C.

The cDNA (complementary DNA) was synthesized from the total RNA by adding the reverse transcriptase (RR036A, PrimeScript™ RT Master Mix, Takara, Japan) according to the protocol provided by the manufacturer. The total RNA was mixed with the 5X PrimeScript RT Master Mix (into final concentration of 1X) and top up with distilled water. Incubated the mixture at 37°C for 15 minutes for the cDNA synthesis and then directly incubated at 85°C for

five seconds to inactivate the enzyme. Measured the amount and purity of DNA by using nanodrop and store the cDNA at freezer until the qPCR is performed.

The expression levels of mRNA (messenger RNA) were evaluated via qPCR (quantitative polymerase chain reaction). For the reaction of qPCR, the cDNA was mixed with the master mix (RR036B, Takara, Japan) and the specific primers. All the primers in this study were designed through Primer-BLAST (basic local alignment search tool) engine of NCBI (National center for biotechnology information) provided by NIH (national institutes of health) and then synthetized via customized orders by IDT (integrated DNA technologies, USA). Then, the mixtures were applied to the 384 well and LightCycler® 480 instrument II (Roche Diagnostics, Switzerland and USA) for the reaction. The relative gene expression levels were calculated by 2^(-ΔΔCt) method according to the reference [70].

Metabolomics

To measure the amounts of metabolites in the hippocampus derived from the glycolytic pathways and TCA cycles, the fresh frozen hippocampus was submitted to the PM-Core (Proteomics and Metabolomics core), CPOS at HKU. For the collection of the hippocampus, the mice were euthanized as described above. The whole hippocampus was isolated from the brain. The isolated hippocampus was stored in 2.0 ml tube added with 500 ul of phosphate-free normal saline at -80℃ until the sample submission for GC-MS/MS (gas chromatography-tandem mass spectrometry) analysis.

The sample processing and GC-MS/MS analysis were performed by PM-CORE, CPOS, HKU. The procedures provided by PM-CORE were summarized here. Each standard reagent of the metabolites, HPLC (high-performance liquid chromatography) grade equivalent or higher, were purchased from different companies. Added 500 μl of methanol/water (80%, v/v)

555 with 200 ng of norvaline as an internal standard to the 50 mg of tissue samples. Homogenized
556 the tissues with probe by sonication. Took the supernatants after centrifugation and the
557 supernatants were dried under gentle stream of nitrogen at room temperature. The dried
558 samples were resuspended with 500 µl of 50% acetonitrile. The samples were vortexed and
559 centrifuged. The supernatants were again dried by a gentle stream of nitrogen at room
560 temperature. The dried residues were redissolved and derivatized into 40 µl of methoxylamine
561 hydrochloride and then added 70 µl MSTFA (N-Methyl-N-(trimethylsilyl) trifluoroacetamide)
562 with 1% TMCS (trimethylchlorosilane for trimethysilyation. Trimethylsilylation is a chemical
563 reaction that replaces a hydrogen atom with trimethylsilyl group (-Si(CH3)3) in a molecule
564 that is for derivatizing the molecules and improving the volatility of the samples for GC-
565 MS/MS analysis. Up to 1 µl of samples were injected into the system, Agilent 7890B GC -
566 Agilent 7010 Triple Quadrapole Mass Spectrometer system (Santa Clara, CA, USA). The
567 samples were separated through the capillary column under constant flow of helium upon the
568 programmed oven with serially increased temperature settings [73].

569 For the calculation of the concentrations of the samples, linear calibration curves for
570 each analyte were generated by integrating the signals, i.e. absorbance, over the peak's width,
571 respectively. The calibration curves of each analyte were used to determine the concentration
572 of unknown samples by comparing them to the known standard concentrations of each
573 metabolite. All the analysis was performed via the Agilent MassHunter Workstation
574 Quantitative Analysis Software.

575

576 **Design of recombinant adeno-associated virus**

577 To detect mitophagy in macrophages and microglia, rAAV was designed. The promoter
578 region of mouse-Iba1 was introduced in the vector that allowed to initiate the gene regulation

or the expression of reporter gene by the rAAV particularly in macrophages and microglia. The mt-mKeima, which was fused with the mitochondria-targeting sequences (tandem repeat of COX VIII) and the dual excitation reporter protein, was applied to the vector. The mKeima is a pH sensitive fluorescence protein derived from stony corals, which has dual excitation wavelengths depending on the pH [74]. In neutral pH, mKeima has excitation wavelengths at 440 nm and emits green light. In an acidic pH, it has excitation wavelengths at 586 nm and emits red light. Thus, mt-mKeima can track whether the mitochondria were delivered to lysosomes, which have an acidic pH, forming from autophagosome (still neural pH) to autolysosomes (an acidic pH).

To downregulate glycolytic enzymes in macrophages and microglia, rAAV was designed. The promoter region of Iba1 and the coding sequences (CDS) of the selected glycolytic enzyme were inserted in the vectors. To downregulate the gene expression levels by adopting the small hairpin RNA structure, miR30 (microRNA 30) was introduced right after the CDS [75].

The rAAVs were designed using the web-based designing tool provided by the VectorBuilder (USA). The customized plasmid of rAAVs were synthesized and packaged at the specialized manufacturing company, a branch of VectorBuilder in Guangzhou, China. The serotype of rAAV for the packing was AAV-PHP.eB, a variant of AAV9, which has higher transduction rates in CNS.

Stereotactic injection

The rAAV was injected into the lateral ventricle (i.c.v, intracerebroventricular injection) via the stereotactic injection system. The stereotactic coordination was adopted from the study investigated in C57BL/6J, 12 weeks old male mice [76]. The coordination of the stereotactic

injection was (x, y, z) = (-1.0, -0.5, -3.0). The stereotaxic frame and instruments were purchased from RWD (RWD Life Sciences, Shenzhen, China). The Hamilton syringe (701RN, Hamilton company, USA and Switzerland) with 26-gauge needle (20793, Hamilton company), which connected to the syringe pump (RWD), was used for the injection. The protocol of the stereotactic injection in this study was written by referencing different studies [77-80]. For the injection, the mouse was anesthetized by KX (i.p).

Liberated the mouse from the stereotactic apparatus. Completed closed the burr hole on the skull with applying a sterilized bone wax (B. Braun, Germany). The incision was sealed by applying veterinary tissue glue (Vetbond tissue adhesive, 3M, USA). The mouse was returned to the home cage with fresh bedding incubated in ICU at the animal surgery room of the Department of Anaesthesiology for two hours and transferred into the ICU at LAU overnight. And then, the mice were housed at the standard condition of LAU until the laparotomy or LPS challenge.

Statistical analysis

For the analysis of data, One-way Analysis of Variance (ANOVA) and the post hoc tests were performed in BioRender. For the presentation of data, box and whisker plots, also known as boxplots, were used in this study.

The z-score is a numerical measurement to describe the relationship of the values to the mean of a group. The z-score is calculated by using the formula, $z = (x - \mu) / \sigma$. In the formula, x is the individual data point, μ (mu) is the mean of the population, and σ (sigma) is the standard deviation of the population.

Acknowledgements

The metabolomics and the primary analysis were performed by PM CORE of CPOS, The University of Hong Kong, Hong Kong, SAR.

The IHC imaging and flow cytometry analysis were performed at the core facilities of Imaging and Flow Cytometry Core of CPOS, The University of Hong Kong, SAR.

Author contributions

Conceptualization: Kate Inyoung OH, Gordon Tin Chun WONG, Raymond Chuen Chung CHANG

Investigation: Kate Inyoung OH, Gordon Tin Chun WONG, Raymond Chuen Chung CHANG

Design recombinant adeno-associated viruses: Kate Inyoung OH

Writing-original draft: Kate Inyoung OH

Writing-review and editing: Kate Inyoung OH, Kornelia GLADYSZ, Jung Sun YOO, Gordon Tin Chun WONG, Raymond Chuen Chung CHANG

Formal analysis: Kate Inyoung OH, Kornelia GLADYSZ

Validation and data curation: Kate Inyoung OH, Kornelia GLADYSZ

Fundings: Kate Inyoung OH, Raymond Chuen Chung CHANG

Supervision: Gordon Tin Chun WONG, Raymond Chuen Chung CHANG

Conflict of Interest

There is no conflict of interest

References

1 Huang, C., Irwin, M. G., Wong, G. T. C. & Chang, R. C. C. Evidence of the impact of systemic inflammation on neuroinflammation from a non-bacterial endotoxin animal model. *J Neuroinflammation* **15**, 147 (2018). https://doi.org:10.1186/s12974-018-1163-z

2 Prinz, M. & Priller, J. The role of peripheral immune cells in the CNS in steady state and disease. *Nature Neuroscience* **20**, 136-144 (2017). https://doi.org:10.1038/nn.4475

3 Park, C. *et al.* Platelet factors are induced by longevity factor klotho and enhance cognition in young and aging mice. *Nature Aging* **3**, 1067-1078 (2023). https://doi.org:10.1038/s43587-023-00468-0

4 Ho, Y. S. *et al.* Postoperative Electroacupuncture Boosts Cognitive Function Recovery after Laparotomy in Mice. *Biomolecules* **14** (2024). https://doi.org:10.3390/biom14101274

5 Cheng, W. Y., Chan, P. L., Ong, H. Y., Wong, K. H. & Chang, R. C. Systemic Inflammation Disrupts Circadian Rhythms and Diurnal Neuroimmune Dynamics. *Int J Mol Sci* **25** (2024). https://doi.org:10.3390/ijms25137458

6 Galea, I. The blood–brain barrier in systemic infection and inflammation. *Cellular & Molecular Immunology* **18**, 2489-2501 (2021). https://doi.org:10.1038/s41423-021-00757-x

7 Kiani Shabestari, S. *et al.* Absence of microglia promotes diverse pathologies and early lethality in Alzheimer's disease mice. *Cell Reports* **39**, 110961 (2022). https://doi.org:https://doi.org/10.1016/j.celrep.2022.110961

8 Fekete, R. *et al*. Microglia dysfunction, neurovascular inflammation and focal neuropathologies are linked to IL-1- and IL-6-related systemic inflammation in COVID-19. *Nature Neuroscience* **28**, 558-576 (2025). https://doi.org:10.1038/s41593-025-01871-z

9 Gao, C., Jiang, J., Tan, Y. & Chen, S. Microglia in neurodegenerative diseases: mechanism and potential therapeutic targets. *Signal Transduction and Targeted Therapy* **8**, 359 (2023). https://doi.org:10.1038/s41392-023-01588-0

10 Fiebich, B. L., Batista, C. R. A., Saliba, S. W., Yousif, N. M. & de Oliveira, A. C. P. Role of Microglia TLRs in Neurodegeneration. *Front Cell Neurosci* **12**, 329 (2018). https://doi.org:10.3389/fncel.2018.00329

11 Todd, L. *et al*. Reactive microglia and IL1β/IL-1R1-signaling mediate neuroprotection in excitotoxin-damaged mouse retina. *Journal of Neuroinflammation* **16**, 118 (2019). https://doi.org:10.1186/s12974-019-1505-5

12 Fritsch, L. E. *et al*. STING-Dependent Signaling in Microglia or Peripheral Immune Cells Orchestrates the Early Inflammatory Response and Influences Brain Injury Outcome. *J Neurosci* **44** (2024). https://doi.org:10.1523/jneurosci.0191-23.2024

13 Baddam, S. & Burns, B. in *StatPearls* (StatPearls Publishing

Copyright © 2025, StatPearls Publishing LLC., 2025).

14 Stec-Martyna, E., Wojtczak, K., Nowak, D. & Stawski, R. Battle of the Biomarkers of Systemic Inflammation. *Biology* **14**, 438 (2025).

15 Tesfaye, Y. *et al*. Long-term clinical outcomes of delirium after hospital discharge: a systematic review and meta-analysis. *Age Ageing* **54** (2025). https://doi.org:10.1093/ageing/afaf188

16 Al-Aly, Z. *et al*. Long COVID science, research and policy. *Nature Medicine* **30**, 2148-2164 (2024). https://doi.org:10.1038/s41591-024-03173-6

17 Zhou, Y. *et al*. Network medicine links SARS-CoV-2/COVID-19 infection to brain microvascular injury and neuroinflammation in dementia-like cognitive impairment. *Alzheimer's Research & Therapy* **13**, 110 (2021). https://doi.org:10.1186/s13195-021-00850-3

18 Bartsch, T. & Wulff, P. The hippocampus in aging and disease: From plasticity to vulnerability. *Neuroscience* **309**, 1-16 (2015). https://doi.org:https://doi.org/10.1016/j.neuroscience.2015.07.084

19 Davidson, T. L. & Stevenson, R. J. Vulnerability of the Hippocampus to Insults: Links to Blood-Brain Barrier Dysfunction. *Int J Mol Sci* **25** (2024). https://doi.org:10.3390/ijms25041991

20 Wendeln, A.-C. *et al*. Innate immune memory in the brain shapes neurological disease hallmarks. *Nature* **556**, 332-338 (2018). https://doi.org:10.1038/s41586-018-0023-4

21 Quintin, J., Cheng, S. C., van der Meer, J. W. & Netea, M. G. Innate immune memory: towards a better understanding of host defense mechanisms. *Curr Opin Immunol* **29**, 1-7 (2014). https://doi.org:10.1016/j.coi.2014.02.006

22 Netea, M. G., Latz, E., Mills, K. H. G. & O'Neill, L. A. J. Innate immune memory: a paradigm shift in understanding host defense. *Nature Immunology* **16**, 675-679 (2015). https://doi.org:10.1038/ni.3178

23 Lau, C. M. *et al*. Epigenetic control of innate and adaptive immune memory. *Nature Immunology* **19**, 963-972 (2018). https://doi.org:10.1038/s41590-018-0176-1

24 Ferreira, A. V., Domiguéz-Andrés, J. & Netea, M. G. The Role of Cell Metabolism in Innate Immune Memory. *J Innate Immun* **14**, 42-50 (2022). https://doi.org:10.1159/000512280

25 Fanucchi, S., Domínguez-Andrés, J., Joosten, L. A. B., Netea, M. G. & Mhlanga, M. M. The Intersection of Epigenetics and Metabolism in Trained Immunity. *Immunity* **54**, 32-43 (2021). https://doi.org:10.1016/j.immuni.2020.10.011

26 Woollacott, I. O. C. *et al*. Microglial burden, activation and dystrophy patterns in frontotemporal lobar degeneration. *Journal of Neuroinflammation* **17**, 234 (2020). https://doi.org:10.1186/s12974-020-01907-0

27 Rim, C., You, M.-J., Nahm, M. & Kwon, M.-S. Emerging role of senescent microglia in brain aging-related neurodegenerative diseases. *Translational Neurodegeneration* **13**, 10 (2024). https://doi.org:10.1186/s40035-024-00402-3

28 Gulen, M. F. *et al*. cGAS–STING drives ageing-related inflammation and neurodegeneration. *Nature* **620**, 374-380 (2023). https://doi.org:10.1038/s41586-023-06373-1

29 Shahidehpour, R. K. *et al*. Dystrophic microglia are associated with neurodegenerative disease and not healthy aging in the human brain. *Neurobiol Aging* **99**, 19-27 (2021). https://doi.org:10.1016/j.neurobiolaging.2020.12.003

30 Hsu, C.-H. *et al*. StainAI: quantitative mapping of stained microglia and insights into brain-wide neuroinflammation and therapeutic effects in cardiac arrest. *Communications Biology* **8**, 462 (2025). https://doi.org:10.1038/s42003-025-07926-y

31 Huang, H. *et al*. Cellular succinate metabolism and signaling in inflammation: implications for therapeutic intervention. *Front Immunol* **15**, 1404441 (2024). https://doi.org:10.3389/fimmu.2024.1404441

32 Zhang, M. *et al*. Attenuated succinate accumulation relieves neuronal injury induced by hypoxia in neonatal mice. *Cell Death Discovery* **8**, 138 (2022). https://doi.org:10.1038/s41420-022-00940-7

33 Li, X. *et al*. Lactate metabolism in human health and disease. *Signal Transduction and Targeted Therapy* **7**, 305 (2022). https://doi.org:10.1038/s41392-022-01151-3

34 Llibre, A., Kucuk, S., Gope, A., Certo, M. & Mauro, C. Lactate: A key regulator of the immune response. *Immunity* **58**, 535-554 (2025). https://doi.org:10.1016/j.immuni.2025.02.008

35 Wang, Y. *et al*. Alpha-ketoglutarate ameliorates age-related osteoporosis via regulating histone methylations. *Nature Communications* **11**, 5596 (2020). https://doi.org:10.1038/s41467-020-19360-1

36 Asadi Shahmirzadi, A. *et al*. Alpha-Ketoglutarate, an Endogenous Metabolite, Extends Lifespan and Compresses Morbidity in Aging Mice. *Cell Metab* **32**, 447-456.e446 (2020). https://doi.org:10.1016/j.cmet.2020.08.004

37 Domínguez-Andrés, J. *et al*. Trained immunity: adaptation within innate immune mechanisms. *Physiological Reviews* **103**, 313-346 (2023). https://doi.org:10.1152/physrev.00031.2021

38 Netea, M. G. *et al*. Trained immunity: A program of innate immune memory in health and disease. *Science* **352**, aaf1098 (2016). https://doi.org:doi:10.1126/science.aaf1098

761 39 Lelios, I. & Greter, M. Trained Microglia Trigger Memory Loss. *Immunity* **48**, 849-
762 851 (2018). https://doi.org:10.1016/j.immuni.2018.04.033
763 40 Netea, M. G. *et al.* Trained Immunity: a Tool for Reducing Susceptibility to and the
764 Severity of SARS-CoV-2 Infection. *Cell* **181**, 969-977 (2020).
765 https://doi.org:10.1016/j.cell.2020.04.042
766 41 Miska, J. *et al.* HIF-1α Is a Metabolic Switch between Glycolytic-Driven Migration
767 and Oxidative Phosphorylation-Driven Immunosuppression of Tregs in
768 Glioblastoma. *Cell Rep* **27**, 226-237.e224 (2019).
769 https://doi.org:10.1016/j.celrep.2019.03.029
770 42 Dong, H. *et al.* Hypoxia inducible factor-1α regulates microglial innate immune
771 memory and the pathology of Parkinson's disease. *Journal of Neuroinflammation*
772 **21**, 80 (2024). https://doi.org:10.1186/s12974-024-03070-2
773 43 Kim, J.-w., Tchernyshyov, I., Semenza, G. L. & Dang, C. V. HIF-1-mediated
774 expression of pyruvate dehydrogenase kinase: A metabolic switch required for
775 cellular adaptation to hypoxia. *Cell Metabolism* **3**, 177-185 (2006).
776 https://doi.org:https://doi.org/10.1016/j.cmet.2006.02.002
777 44 Papandreou, I., Cairns, R. A., Fontana, L., Lim, A. L. & Denko, N. C. HIF-1 mediates
778 adaptation to hypoxia by actively downregulating mitochondrial oxygen
779 consumption. *Cell Metabolism* **3**, 187-197 (2006).
780 https://doi.org:10.1016/j.cmet.2006.01.012
781 45 Yang, Y. & Gibson, G. E. Succinylation Links Metabolism to Protein Functions.
782 *Neurochem Res* **44**, 2346-2359 (2019). https://doi.org:10.1007/s11064-019-
783 02780-x

46 Zhao, X. *et al*. Up-regulated succinylation modifications induce a senescence phenotype in microglia by altering mitochondrial energy metabolism. *J Neuroinflammation* **21**, 296 (2024). https://doi.org:10.1186/s12974-024-03284-4

47 Weyh, M., Jokisch, M.-L., Nguyen, T.-A., Fottner, M. & Lang, K. Deciphering functional roles of protein succinylation and glutarylation using genetic code expansion. *Nature Chemistry* **16**, 913-921 (2024). https://doi.org:10.1038/s41557-024-01500-5

48 Yang, Y. *et al*. Altered succinylation of mitochondrial proteins, APP and tau in Alzheimer's disease. *Nat Commun* **13**, 159 (2022). https://doi.org:10.1038/s41467-021-27572-2

49 Acosta, D. M., Mancinelli, C., Bracken, C. & Eliezer, D. Post-translational modifications within tau paired helical filament nucleating motifs perturb microtubule interactions and oligomer formation. *J Biol Chem* **298**, 101442 (2022). https://doi.org:10.1016/j.jbc.2021.101442

50 Acosta, D. M. & Eliezer, D. Biophysical Characterization of Covalently Modified Protein Tau: Oligomers, Aggregation, and Tubulin Interactions. *Biophysical Journal* **118**, 58a-59a (2020). https://doi.org:10.1016/j.bpj.2019.11.497

51 Yang, Y. *et al*. Altered succinylation of mitochondrial proteins, APP and tau in Alzheimer's disease. *Nature Communications* **13**, 159 (2022). https://doi.org:10.1038/s41467-021-27572-2

52 Ashrafi, G. & Schwarz, T. L. The pathways of mitophagy for quality control and clearance of mitochondria. *Cell Death & Differentiation* **20**, 31-42 (2013). https://doi.org:10.1038/cdd.2012.81

53 Ma, K. *et al*. Mitophagy, Mitochondrial Homeostasis, and Cell Fate. *Front Cell Dev Biol* **8**, 467 (2020). https://doi.org:10.3389/fcell.2020.00467

54 Collier, J. J., Oláhová, M., McWilliams, T. G. & Taylor, R. W. Mitochondrial signalling and homeostasis: from cell biology to neurological disease. *Trends Neurosci* **46**, 137-152 (2023). https://doi.org:10.1016/j.tins.2022.12.001

55 Norat, P. *et al*. Mitochondrial dysfunction in neurological disorders: Exploring mitochondrial transplantation. *npj Regenerative Medicine* **5**, 22 (2020). https://doi.org:10.1038/s41536-020-00107-x

56 Wang, W. *et al*. Endonuclease G promotes autophagy by suppressing mTOR signaling and activating the DNA damage response. *Nature Communications* **12**, 476 (2021). https://doi.org:10.1038/s41467-020-20780-2

57 Dahal, S. *et al*. Unleashing a novel function of Endonuclease G in mitochondrial genome instability. *Elife* **11** (2022). https://doi.org:10.7554/eLife.69916

58 Lodge, M. *et al*. Fructose regulates the pentose phosphate pathway and induces an inflammatory and resolution phenotype in Kupffer cells. *Scientific Reports* **14**, 4020 (2024). https://doi.org:10.1038/s41598-024-54272-w

59 Yi, W. *et al*. Phosphofructokinase 1 glycosylation regulates cell growth and metabolism. *Science* **337**, 975-980 (2012). https://doi.org:10.1126/science.1222278

60 Bonvento, G. & Bolaños, J. P. Astrocyte-neuron metabolic cooperation shapes brain activity. *Cell Metabolism* **33**, 1546-1564 (2021). https://doi.org:https://doi.org/10.1016/j.cmet.2021.07.006

61 Beard, E., Lengacher, S., Dias, S., Magistretti, P. J. & Finsterwald, C. Astrocytes as Key Regulators of Brain Energy Metabolism: New Therapeutic Perspectives. *Front Physiol* **12**, 825816 (2021). https://doi.org:10.3389/fphys.2021.825816

62 Yang, H. *et al*. Microglia lactylation in relation to central nervous system diseases. *Neural Regen Res* **20**, 29-40 (2025). https://doi.org:10.4103/nrr.Nrr-d-23-00805

63 Ge, X. *et al*. Metabolic reprogramming through histone lactylation in microglia and macrophages recruits CD8+ T lymphocytes and aggravates spinal cord injury. *Neuron* (2025). https://doi.org:https://doi.org/10.1016/j.neuron.2025.04.003

64 Hu, X. *et al*. Lactate promotes microglial scar formation and facilitates locomotor function recovery by enhancing histone H4 lysine 12 lactylation after spinal cord injury. *Journal of Neuroinflammation* **21**, 193 (2024). https://doi.org:10.1186/s12974-024-03186-5

65 Ziogas, A. *et al*. Long-term histone lactylation connects metabolic and epigenetic rewiring in innate immune memory. *Cell* **188**, 2992-3012.e2916 (2025). https://doi.org:10.1016/j.cell.2025.03.048

66 Cai, H. *et al*. Lactate activates trained immunity by fueling the tricarboxylic acid cycle and regulating histone lactylation. *Nature Communications* **16**, 3230 (2025). https://doi.org:10.1038/s41467-025-58563-2

67 Wang, X. *et al*. H4K12 Lactylation Activated-Spp1 in Reprogrammed Microglia Improves Functional Recovery After Spinal Cord Injury. *CNS Neurosci Ther* **31**, e70232 (2025). https://doi.org:10.1111/cns.70232

68 Moberg, I. *et al*. Lactate increases ADAM10 activity and reduces BACE1 activity in mouse brain. *J Physiol* **602**, 5217-5228 (2024). https://doi.org:10.1113/jp286962

69 Huang, C., Chu, J. M.-T., Liu, Y., Chang, R. C.-C. & Wong, G. T.-C. Varenicline reduces DNA damage, tau mislocalization and post surgical cognitive impairment in aged mice. *Neuropharmacology* **143**, 217-227 (2018). https://doi.org:https://doi.org/10.1016/j.neuropharm.2018.09.044

70 Livak, K. J. & Schmittgen, T. D. Analysis of Relative Gene Expression Data Using Real-Time Quantitative PCR and the 2−ΔΔCT Method. *Methods* **25**, 402-408 (2001). https://doi.org:https://doi.org/10.1006/meth.2001.1262

71 Bourges, I. *et al*. Structural organization of mitochondrial human complex I: role of the ND4 and ND5 mitochondria-encoded subunits and interaction with prohibitin. *Biochem J* **383**, 491-499 (2004). https://doi.org:10.1042/bj20040256

72 Houštek, J. *et al*. Nonsynonymous variants in mt-Nd2, mt-Nd4, and mt-Nd5 are linked to effects on oxidative phosphorylation and insulin sensitivity in rat conplastic strains. *Physiol Genomics* **44**, 487-494 (2012). https://doi.org:10.1152/physiolgenomics.00156.2011

73 Roessner, U. *et al*. An investigation of boron toxicity in barley using metabolomics. *Plant Physiol* **142**, 1087-1101 (2006). https://doi.org:10.1104/pp.106.084053

74 Kogure, T. *et al*. A fluorescent variant of a protein from the stony coral Montipora facilitates dual-color single-laser fluorescence cross-correlation spectroscopy. *Nature Biotechnology* **24**, 577-581 (2006). https://doi.org:10.1038/nbt1207

75 Chang, K., Marran, K., Valentine, A. & Hannon, G. J. Creating an miR30-based shRNA vector. *Cold Spring Harb Protoc* **2013**, 631-635 (2013). https://doi.org:10.1101/pdb.prot075853

874 76 Taylor, Z. V., Khand, B., Porgador, A., Monsonego, A. & Eremenko, E. An optimized
875 intracerebroventricular injection of CD4(+) T cells into mice. *STAR Protoc* **2**,
876 100725 (2021). https://doi.org:10.1016/j.xpro.2021.100725
877 77 Baumann, B. C., Dorsey, J. F., Benci, J. L., Joh, D. Y. & Kao, G. D. Stereotactic
878 intracranial implantation and in vivo bioluminescent imaging of tumor xenografts
879 in a mouse model system of glioblastoma multiforme. *J Vis Exp* (2012).
880 https://doi.org:10.3791/4089
881 78 Candolfi, M. *et al*. Intracranial glioblastoma models in preclinical neuro-oncology:
882 neuropathological characterization and tumor progression. *J Neurooncol* **85**, 133-
883 148 (2007). https://doi.org:10.1007/s11060-007-9400-9
884 79 Zhao, J. *et al*. Neuroinflammation induced by lipopolysaccharide causes cognitive
885 impairment in mice. *Scientific Reports* **9**, 5790 (2019).
886 https://doi.org:10.1038/s41598-019-42286-8
887 80 Huang, M. *et al*. Dual-modality micro-positron emission tomography/computed
888 tomography and near-infrared fluorescence imaging of EphB4 in orthotopic
889 glioblastoma xenograft models. *Mol Imaging Biol* **16**, 74-84 (2014).
890 https://doi.org:10.1007/s11307-013-0674-3
891

892 **Figure legends**

893 **Fig 1. Activation of macrophages/microglia and metabolic changes in the hippocampus**
894 **after the first or second sterile systemic inflammation.** (A) Sterile systemic inflammation
895 was induced in C57BL/6J, 4-6 months of male mice via conducting laparotomy under
896 sevoflurane one or twice. The second laparotomy was conducted 28 days after the first
897 operation. The hippocampus was collected for further analysis on POD 14 (n = 6) after the first
898 or second laparotomy, respectively. Before euthanizing the mice, behavior tests were conducted
899 for three consecutive days. (B) Open field and novel object recognition tests after one or twice
900 of sterile systemic inflammation. The red color represents high locomotor activities and
901 movements and yellow to green color illustrates low activities and movements. The blue area
902 means the mice did not stay on the spot during the recording. The global activity and latency
903 of time were analyzed by using SMART3. (C) Expression levels of mRNA were measured by
904 qRT-PCR for the activated macrophages/microglia in the hippocampus after sterile systemic
905 inflammation. 4 batches, 4 mice combined/batch. LightCycler 480, Roche. ACTB (beta-actin),
906 Adgre1 (F4/80, adhesion G protein-coupled receptor E1), STAT (signal transducer and
907 activator of transcription), CD (cluster of differentiation), IL6 (interleukin-6), TNFα (tumor
908 necrosis factor-alpha), Fgf2 (fibroblast growth factor-2), ARG1 (arginase-1), Retnla (fizz1,
909 resistin like alpha). (D) The metabolites from the hippocampus (HP) were analyzed (4
910 combined hippocampus from 2 mice/sample) by using GC-MS/MS (gas chromatography-
911 tandem mass spectrometry). The numbers in the boxes depicted the absolute value of
912 concentration (nmol/g) of the metabolites. z score = $(x - \mu) / \sigma$, x: observed value, μ: mean
913 value of group, σ: standard deviations from the mean. (E) Glycolytic enzyme expression levels,
914 mRNA, in the hippocampus. (F) Schematic diagram of the enhanced (red) or downregulated
915 (blue) metabolites and glycolytic enzyme expressions of the hippocampus after sterile systemic
916 inflammation. One-way ANOVA and Tukey.

Fig 2. Activation of macrophages/microglia and metabolic changes in the hippocampus after the first or second non-sterile systemic inflammation. (A) Non-sterile systemic inflammation was induced in C57BL/6J, 4-6 months of male mice by LPS challenges (i.p) one or twice. The second injection was 28 days after the first injection. The hippocampi were collected on PID 14 (n = 6) after the final injection, respectively, for further analysis. Before euthanizing mice, behavior tests were conducted. (B) The activity and movement were recorded by video and measured by near-infrared count. The global activity was measured and analyzed by using SMART3. (C) The activated inflammatory factors, mRNA levels, were measured by qRT-PCR in the hippocampus after one or twice of LPS challenges. 4 batches, 4 mice combined/batch. (D) Metabolites of glycolysis and pentose phosphate pathways in the hippocampus after non-sterile inflammation. The metabolites from the hippocampus (HP) were analyzed (n = 3) by using GC-MS/MS. (E) The graphs were generated from the concentration of metabolites (n = 3). (F) Glycolytic enzymes expression levels, mRNA, in the hippocampus after non-sterile systemic inflammation. 3 batches, 3 mice combined/batch. (G) The schematic diagram was generated according to the upregulated (red) or downregulated (blue) metabolites and glycolytic enzymes after non-sterile systemic inflammation. One-way ANOVA and Tukey.

Fig 3. Detection of mitochondrial and DNA damages in the hippocampus after sterile or non-sterile systemic inflammation. Recombinant adeno-associated virus (rAAV) was designed to detect mitophagy (mt-mKeima) in microglia (Iba1). The rAAV was administered via the intracerebroventricular (i.c.v) injection. 14 days after the rAAV administration, (A and C) non-sterile inflammation was induced by injecting LPS (i.p) in the mice, or (B and D) sterile systemic inflammation was induced by conducting laparotomy under sevoflurane. The hippocampi were collected on PID 14/POD 14 for the immunohistochemical analysis. (A and B) The brain sections were stained with Hoechst (nucleus, blue) and anti-γH2AX(Ser140)-

Rabbit 647 (double stranded DNA breakages, magenta) (n=3). (C and D) The brain sections were stained with Hoechst (nucleus, blue) and H4K12la-Rabbit 647 (histone lactylation, magenta) (n=3). The green and red channels detected the signals of mt-mKeima. The images were taken by the confocal microscope, LSM 800, 40x oil lens, 17 of z stacks (1 μm distance). Merged and enlarged images, and the images from the single channels.

Fig 4. Downregulation of the enhanced glycolysis on neuroimmune responses triggered by sterile systemic inflammation. (A) Selection of two glycolytic enzymes to downregulate the shifting of glycolysis in the hippocampus. The red colored metabolites were significantly increased in the hippocampus after sterile or non-sterile systemic inflammation. The two glycolytic enzymes were selected for designing rAAV targeting microglia (Iba1+). (B) The rAAV-Iba1-shPfk1/shPfk2 was injected (i.c.v) into the mice. 14 days after the rAAV administration, sterile systemic inflammation was induced by conducting laparotomy under sevoflurane one or twice. The hippocampi were collected on POD 14 after the final laparotomy, respectively. (C) Metabolites from the hippocampus after sterile systemic inflammation under the manipulated levels of glycolytic enzymes in microglia. The red colored metabolites (left row) were significantly increased after sterile inflammation (n = 3). The heatmap was generated according to the z scores. The numbers in the boxes are the absolute values of the concentration of the metabolites (nmol/sample). (D) The graphs represent the concentration of glycolytic metabolites, glucose-6-phosphate and fructose-6-phosphate, upon downregulation of microglial Pfk1 or Pfk2 after sterile systemic inflammation. The rAAV-Iba1-shPfk1/Pfk2 as well as rAAV-Iba1-mt-mKeima were co-injected 14 days prior to the first sterile systemic inflammation. The brain sections were stained with Hoechst (blue) and anti-γH2AX (DNA damages, magenta) (E) after the first sterile systemic inflammation or (F) after the second sterile systemic inflammation. The green channel was for detecting the fluorescence from the

rAAV under the gene expressions (n = 3). LSM 800, 40x oil lens, total 17 stacks with 1 μm distance. Scale bar is 15 μm. (G) The ratio of mKeima-red after sterile systemic inflammation. (H) The ratio of mKeima-red after downregulating microglia Pfk1 or Pfk2 in the mice. The MFIs of Fig 4.g and 4.h were measured from each stack, 17 stacks x 6 slices x 3 mice per group. (I) The MFI of γH2AX in the hippocampus after sterile systemic inflammation. (J) The MFI of γH2AX in the hippocampus upon the downregulation of microglial Pfk1 or Pfk2. The MFIs of Fig 4.I and 4.J were measured from each stack,17 stacks x 3 mice per group. (K) Flow cytometry analysis for detecting DNA damage after sterile systemic inflammation in the rAAV injected mice. The isolated cells from the hippocampus were stained with anti-CD45-BV650 and anti-γH2AX-Rabbit 647 antibodies for flow cytometry analysis (3 combined mice/batch, one batch, 3-9 reading of the pool). (L) The MFI of γH2AX immunoreactivity and the number of cells among CD45+ cells in the hippocampus. (M) The isolated cells from the hippocampus were stained with anti-CD45-BV650 and anti-H4K12la-Rabbit 647 antibodies for flow cytometry analysis (3 combined mice/batch, one batch, 3-9 reading of the pool). (N) The MFI of H4K12la immunoreactivity and the number of cells in the hippocampus. One-way ANOVA and Tukey.

Fig 5. Effects of downregulation of microglial glycolytic enzymes on the innate immune reactions in the hippocampus after sterile systemic inflammation. The brain sections were stained with Hoechst (blue) anti-Iba1-Rabbit 647 (magenta) (A) after the first sterile systemic inflammation or (B) after the second sterile systemic inflammation. The green, red and the merged channels were for detecting the excitation signals from Iba1-mt-mKeima (n = 3). LSM 800, 40x oil lens, total 17 stacks with 1 μm distance. Scale bar is 15 μm. (C) The MFI of Iba1 in the hippocampus after sterile systemic inflammation. (D) The MFI of Iba1 after downregulation of microglial glycolytic enzymes. (E) The MFI of P2RY12 in the hippocampus

after sterile systemic inflammation. (F) The MFI of P2RY12 after downregulation of the enzymes. The MFIs were measured from each stack, 17 stacks x 3 mice per group. (G) The isolated cells from the hippocampus were co-stained with anti-CD11b-APC/Cy7 and anti-CD45-BV650 for flow cytometry analysis (H) The MFI and the number of microglia ($CD11b^{+}CD45^{low}$) and macrophage-like cells ($CD11b^{+}CD45^{high}$). (I) The isolated cells stained with anti-CD45-BV650 and anti-STING-647 and (J) the MFI and the number of cells analyzed by flow cytometry. (K) The isolated cells stained with anti-CD11b-APC/Cy7 and anti-CD121a-PE and (L) the MFI and the number of cells analyzed by flow cytometry. 3 combined mice/batch, one batch, 3-9 reading of the pool. One-way ANOVA and Tukey.

Fig 6. Downregulation of phosphofructokinase in microglia altered the neuroimmune responses after non-sterile systemic inflammation. (A) After 14 days of rAAV-Iba1-shPfk1/Pfk2 administration (i.c.v), LPS was injected intraperitoneally (i.p). On PID 14 after the LPS challenge, the hippocampi were collected for further analysis. (B) Metabolites after non-sterile systemic inflammation under the modulation of microglial glycolytic enzyme levels. The red colored metabolites (left row) were significantly increased after sterile inflammation (n = 3). The heatmap was generated according to the z scores. The numbers in the boxes are the absolute values of the concentration of the metabolites in the hippocampus. The white empty boxes depicted non-detectable (ND) values. (C) The concentration of metabolites from the hippocampus. The graphs generated from Fig 6.b. The rAAV-Iba1-shPfk1/Pfk2 as well as rAAV-Iba1-mt-mKeima were co-injected 14 days prior to the first LPS challenge. The brain sections were collected stained with Hoechst (blue) and anti-γH2AX-Rabbit 647 (magenta) (D) 14 days after the first LPS challenge (i.p) or (E) after the second LPS challenge. The green, red and the merged channels were for detecting the excitation signals from Iba1-mt-mKeima (n = 3). LSM 800, 40x oil lens, total 17 stacks with 1 µm distance. Scale bar is 15 µm. (F) The ratio

of mKeima-red after non-sterile systemic inflammation. (G) The ratio of mKeima-red after downregulating microglial Pfk1 or Pfk2 in the mice. The MFIs of Fig 4.f and 4.g were measured from each of 17 stacks, 17 x 6 slices x 3 mice per group. (H) The MFI of γH2AX in the hippocampus after non-sterile systemic inflammation. (I) The MFI of γH2AX in the hippocampus upon the downregulation of microglial Pfk1 or Pfk2. The MFIs of Fig 4.h and 4.i were measured from each stack, 17 stacks x 3 mice per group. (J) The isolated cells from the hippocampus were stained with anti-CD45-BV650 and anti-γH2AX-Rabbit 647 for flow cytometry analysis (3 combined mice/batch, one batch, 3-9 reading). (K) The MFI of γH2AX immunoreactivity among CD45+ cells and the number of cells in the hippocampus. (L) The isolated cells from the hippocampus co-stained with anti-CD45-BV650 and anti-H4K12la-Rabbit 647 for flow cytometry analysis (3 combined mice/batch, one batch, 3-9 reading). (M) The MFI and the number of cells among CD45+ cells. One-way ANOVA and Tukey.

Fig 7. Effects of downregulation of microglial glycolytic enzymes on the innate immune reactions in the hippocampus after non-sterile systemic inflammation. The rAAV-Iba1-shPfk1/Pfk2 and rAAV-Iba1-mt-mKeima were co-injected 14 days prior to the first LPS challenge. The brain sections were collected stained with Hoechst (blue) and anti-Iba1-Rabbit 647 (magenta) (A) 14 days after the first LPS challenge (i.p) or (B) the second LPS challenge. (C) The MFI of Iba1 in the hippocampus after the non-sterile systemic inflammation. (D) The MFI of Iba1 after downregulation of microglial glycolytic enzymes. (E) The MFI of P2RY12 in the hippocampus after the non-sterile systemic inflammation. (F) The MFI of P2RY12 after downregulating the enzymes. The MFIs were measured from each stack, 17 stacks x 3 mice per group. (G) The isolated cells from the hippocampus were co-stained with anti-CD11b-APC/Cy7 and anti-CD45-BV650 for flow cytometry analysis. 3 separated staining from 3 combined mice/batch, one batch, 3 readings of the pools. The isolated cells from the

hippocampus of 2x LPS groups were unable to read due to the poor population of the cells after the initial gatings for singlets by FSC/SSC and CD45/CD11b, which was consistent with the poor immunoreactivity of Iba1 after the second LPS challenges in Fig 7.b. (H) The population of microglia or macrophages-like cells after downregulation of the enzymes. (I) The population of CD11b+CD45low and CD11b+CD45high cells were analyzed in comparison the effects of the rAAVs in the groups. (I) The isolated cells from the hippocampus were stained with anti-CD45-BV650 and anti-STING-647 for flow cytometry analysis. 3 combined mice/batch, one batch, 3-9 reading of the pool. (J) The MFI of STING immunoreactivity among CD45+ cells and the number of cells. (K) The isolated cells from the hippocampus were stained with anti-CD11b-APC/Cy7 and anti-CD121a-PE antibodies for flow cytometry analysis. 3 combined mice/batch, one batch, 3-9 reading of the pool. (L) The MFI of CD121a immunoreactivity among CD11b+ cells, and the number of cells. One-way ANOVA and Tukey.

Fig 8. Schematic diagram of the hypothesis how mitochondrial damage induces nuclear DNA damage followed by the subsequent pro-inflammatory innate immune reactions in microglia. Systemic inflammation can alter the integrity of BBB facilitating the infiltration of pro-inflammatory immune insults into the brain. In turn, microglia can be activated with metabolic changes. Various immune insults can damage mitochondria leading to the leakage of mtDNA (mitochondrial DNA) and other proteins including endonuclease G. The endonuclease G can enter into nucleus causing nDNA (nuclear DNA) fragmentation. The released mtDNA and nDNA in cytosol are detected by cGAS (cyclic GMP-AMP synthase) leading to the activation of STING (stimulator of interferon genes) on ER (endoplasmic reticulum). In turn, STING activates NLRP3 (NOD-like receptor protein-3) inflammasome triggering the activation of caspase-1. The activated caspase-1 cleaves pro-IL-1β, pro-IL-18 and gasdermin D into their active forms. The activated gasdermin D generates pores on the cell

membrane leading to pyroptosis, a cell death. IL-1β and IL-18 are secreted to bind the specific receptors, respectively. IL-1β binds to CD121a (IL-1R1, IL-1 receptor type 1). Activated CD121a recruits MyD88 (myeloid differentiation primary response gene 88) triggering the pro-inflammatory signaling pathways including NF-κB (nuclear factor kappa B) and MAPK (mitogen-activated protein kinases). It leads to additional mitochondrial damage activating STING signaling pathway. Leaked damaged mitochondria, mtDNA and nDNA can be cleared by autophagosome to autolysosome. The overwhelmed mitochondrial damage can prevail in the capacity of clearing and buffering of the cell leading to mitochondrial dysfunction and the metabolic imbalance. It can further lead to neuronal damage.

Figure legends of supplementary figures

Fig S1. The hippocampus of mice (A) the days after sevoflurane, and (B) the days after laparotomy under sevoflurane, respectively, were stained with Hoechst (nucleus, blue), Iba1-Rabbit 488 (activated microglia, green), GFAP-mouse 568 (activated astrocytes, red) and STING-647 (stimulator of interferon genes, magenta) (n = 3). From the left, there are merged images of all channels, enlarged images (4x, yellow box) of area of interest, blue, green, red and far-red channels, respectively. In the enlarged images, the brighter magenta-colored (pseudo color) dots in the cell body of microglia represent STING positive signals.

The hippocampus of mice (C) the days after sevoflurane, and (D) the days after laparotomy under sevoflurane, respectively, was stained with Hoechst (nucleus, blue), γH2AX-Rabbit 488 (double stranded DNA breakages, green), mitoTracker Red (mitochondria, red) and P2RY12-Guinepig 647 (purinergic receptor P2Y, magenta). From the left, there are merged images of all channels, enlarged images (4x, yellow box) of area of interest, blue, green, red and far-red channels, respectively. In the enlarged images, green-colored dots are double-stranded DNA

breakages around the homeostatic microglia (magenta) (n = 3). The images were taken under the confocal laser scanning microscope, LSM 800, Zeiss with 40x oil lens, z stacks (1.0 μm of distance, total 17 of z stacks). The scale bar is 15 μm.

Fig S2. (A) The brain sections were examined by Hoechst (nucleus, blue), Iba1-Rabbit 488 (activated microglia, green), mitoTracker Red (mitochondria, red) and STING-647 (stimulator of interferon genes, magenta). The left image of normal saline (1x NS) was taken by the two-photon laser scanning confocal microscope, LSM 780, Zeiss with 20x lens, z stacks (1.0μm of distance, total 20 of z stacks). The scale bar is 20μm. The middle and right images of LPS (1x LPS, 48 hr and 72 hr) were taken under LSM 800, Zeiss with 40x oil lens, z stacks (1.0 μm of distance, total 17 of z stacks). The scale bar is 15 μm. In the enlarged images, the brighter magenta-colored (pseudo color) or white dots in the cell body of microglia represent STING positive immunoreactivity. (B) The hippocampus was stained with Hoechst (nucleus, blue), anti-Iba1-Rabbit 488 (activated microglia, green) and anti-CD121a-PE (IL1R1; IL1R-alpha, Interleukin-1 receptor type I, red) (n = 3). The images were taken by the two-photon laser scanning confocal microscope, LSM 780, Zeiss with 40x oil lens, z stacks (0.5 μm of distance, total 20 of z stacks). The scale bar is 20μm. The merged (the first line) and enlarged (the second line) images. (C) The whole brain sections were stained with Hoechst (nucleus, blue), Iba1-Rabbit 488 (activated microglia, green), GFAP-mouse 568 (activated astrocytes, red), pSTING-488 (phospho-STING, Ser366, green), calnexin-568 (activated endoplasmic reticulum, red) and STING-647 (stimulator of interferon genes, magenta) (n = 3). The images were taken under the inverted wide field fluorescence microscope, Ti2-E, Nikon with 20x lens, tile scan. (D) The whole brain sections were stained with Hoechst (nucleus, blue), anti-Iba1-Rabbit 488 (activated microglia, green), anti-GFAP-mouse 568 (activated astrocytes, red) and anti-STING-647 (stimulator of interferon genes, magenta) (n = 3). The images were taken by

the two-photon laser scanning confocal microscope, LSM 780, Zeiss with 20x lens, z stacks (1.0μm of distance, total 20 of z stacks). The scale bar is 50 μm. (E) Microglia ($CD11b^{+}CD45^{low}$) and macrophage-like cells ($CD11b^{+}CD45^{high}$) were sorted by using flow cytometry, BD Fusion, BD. RNA was extracted from the sorted cells and the mRNA expression levels measured by qRT-PCR, LightCycler 480, Roche. 4 batches, 4 mice combined/batch. The relative mRNA expression levels of the activated macrophages and microglia markers of (F) pro-inflammatory and (i) anti-inflammatory states. Adgre1: F4/80, adhesion G protein-coupled receptor E1 / CCR2 (C-C chemokine receptor type 2), CD (cluster of differentiation), TNFα: tumor necrosis factor-alpha, STAT (signal transducer and activator of transcription), NOS (inducible nitric oxide synthase, iNOS), Ifnar1 (type I interferon receptor complex), STING (stimulator of interferon genes), ARG1 (arginase-1), IL10 (interleukin-10), Retnla (fizz1, resistin like alpha).

The cells from the hippocampus stained with Hoechst, CD11b-APC/Cy7, CD45-BV650 and mitoTracker-Red for flow cytometry and confocal microscopy. (G) The fluorescence intensity of mitoTracker-Red was evaluated from CD11b+CD45+ cells, and the cells were observed under the confocal microscope (LSM 800). (H) DNA was extracted from the sorted cells for measuring mtDNA copy number by using PCR (LightCycler 480, Roche).

Cellular and Molecular Immunology

Figures in the manuscript

Title of manuscript:

Glycolytic enzymes play important roles in innate immune memory of neuroimmune responses triggered by systemic inflammation

Kate Inyoung OH

Fig 1

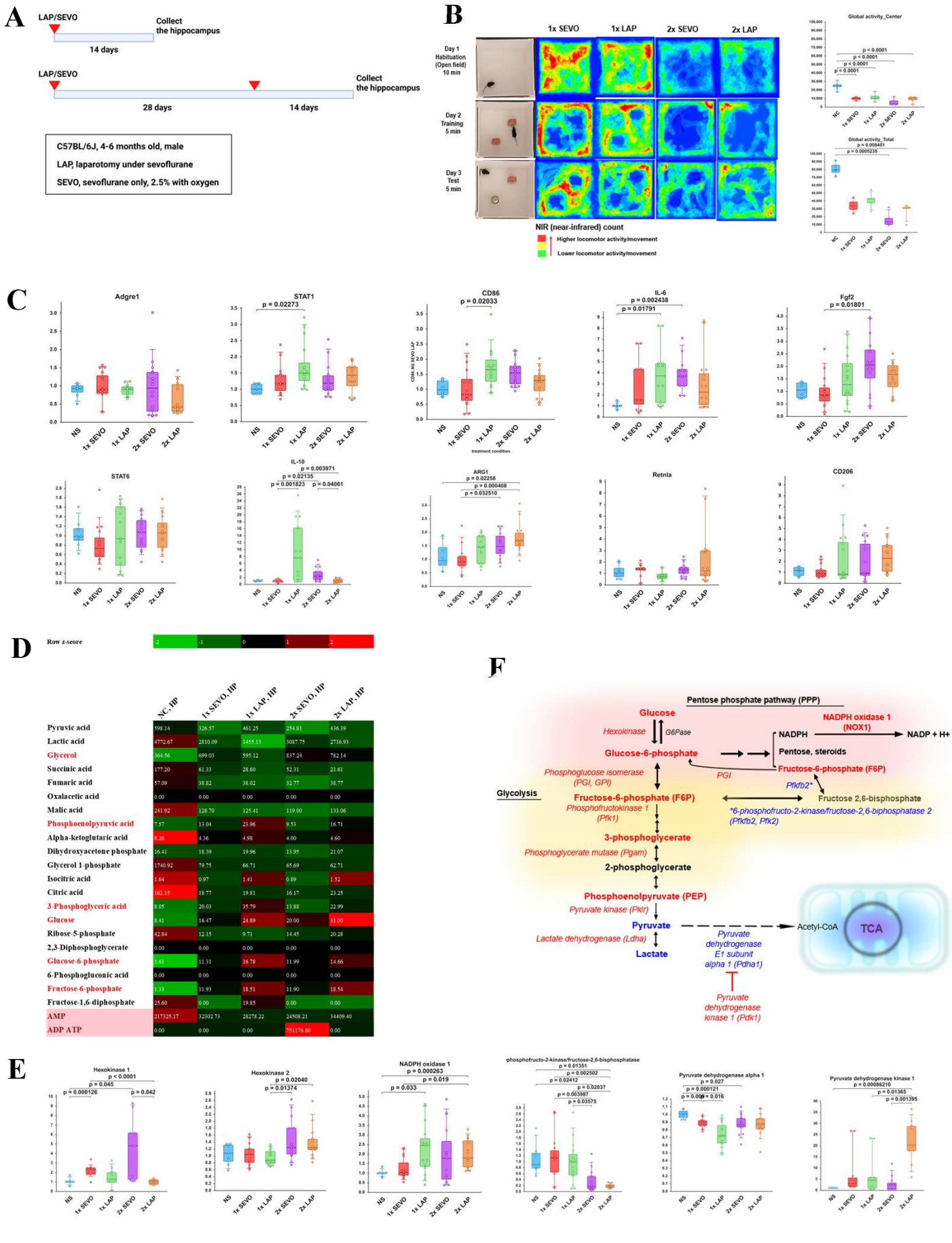

A
LAP/SEVO
Collect the hippocampus
14 days
LAP/SEVO
Collect the hippocampus
28 days
14 days
C57BL/6J, 4-6 months old, male
LAP, laparotomy under sevoflurane
SEVO, sevoflurane only, 2.5% with oxygen
B
1x SEVO
1x LAP
2x SEVO
2x LAP
Day 1 Habituation (Open field) 10 min
Day 2 Training 5 min
Day 3 Test 5 min
NIR (near-infrared) count
Higher locomotor activity/movement
Lower locomotor activity/movement
Global activity_Center
Global activity_Total
C
Adgre1
STAT1
p = 0.02273
CD86
p = 0.02033
IL-6
p = 0.002438
p = 0.01791
Fgf2
p = 0.01801
STAT6
IL-10
p = 0.003971
p = 0.02135
p = 0.001823
p = 0.04061
ARG1
p = 0.02258
p = 0.000408
p = 0.032510
Retnla
CD206
NS
1x SEVO
1x LAP
2x SEVO
2x LAP
treatment condition
D
Row z-score
-2
-1
0
1
2
NC, HP
1x SEVO, HP
1x LAP, HP
2x SEVO, HP
2x LAP, HP
Pyruvic acid 598.14 326.57 461.25 254.81 436.39
Lactic acid 4772.67 2810.09 1455.13 3087.75 2716.93
Glycerol 364.56 699.03 595.12 837.24 782.14
Succinic acid 177.20 61.33 28.60 52.31 21.61
Fumaric acid 57.09 38.82 38.02 32.77 38.77
Oxalacetic acid 0.00 0.00 0.00 0.00 0.00
Malic acid 241.92 128.70 125.41 119.00 133.06
Phosphoenolpyruvic acid 7.57 13.04 23.96 9.53 16.71
Alpha-ketoglutaric acid 8.26 4.36 4.98 4.00 4.60
Dihydroxyacetone phosphate 16.41 18.39 19.96 13.95 21.07
Glycerol 1-phosphate 1740.92 79.75 66.71 65.69 62.71
Isocitric acid 1.64 0.97 1.41 0.89 1.52
Citric acid 162.15 18.77 19.81 16.17 23.25
3-Phosphoglyceric acid 8.05 20.03 35.79 13.88 22.99
Glucose 8.41 16.47 24.89 20.00 31.00
Ribose-5-phosphate 42.84 12.15 9.71 14.45 20.28
2,3-Diphosphoglycerate 0.00 0.00 0.00 0.00 0.00
Glucose-6-phosphate 1.61 11.31 16.78 11.99 14.66
6-Phosphogluconic acid 0.00 0.00 0.00 0.00 0.00
Fructose-6-phosphate 1.33 11.93 18.51 11.90 18.54
Fructose-1,6-diphosphate 25.60 0.00 19.85 0.00 0.00
AMP 217325.17 32302.73 28278.22 24508.21 34409.40
ADP ATP 0.00 0.00 0.00 751176.80 0.00
F
Pentose phosphate pathway (PPP)
Glucose
Hexokinase
G6Pase
NADPH oxidase 1 (NOX1)
NADPH
NADP + H+
Glucose-6-phosphate
Pentose, steroids
Phosphoglucose isomerase (PGI, GPI)
PGI
Fructose-6-phosphate (F6P)
Glycolysis
Pfkfb2*
Fructose-6-phosphate (F6P)
Phosphofructokinase 1 (Pfk1)
Fructose 2,6-bisphosphate
*6-phosphofructo-2-kinase/fructose-2,6-biphosphatase 2 (Pfkfb2, Pfk2)
3-phosphoglycerate
Phosphoglycerate mutase (Pgam)
2-phosphoglycerate
Phosphoenolpyruvate (PEP)
Pyruvate kinase (Pklr)
Pyruvate
Acetyl-CoA
TCA
Lactate dehydrogenase (Ldha)
Lactate
Pyruvate dehydrogenase E1 subunit alpha 1 (Pdha1)
Pyruvate dehydrogenase kinase 1 (Pdk1)
E
Hexokinase 1
p < 0.0001
p = 0.045
p = 0.000126
p = 0.042
Hexokinase 2
p = 0.02040
p = 0.01374
NADPH oxidase 1
p = 0.000263
p = 0.019
p = 0.033
6-phosphofructo-2-kinase/fructose-2,6-bisphosphatase
p = 0.01351
p = 0.002502
p = 0.02412
p = 0.02037
p = 0.003987
p = 0.03575
Pyruvate dehydrogenase alpha 1
p = 0.027
p = 0.000121
p = 0.009
p = 0.016
Pyruvate dehydrogenase kinase 1
p = 0.00086210
p = 0.01365
p = 0.001395

Fig 2

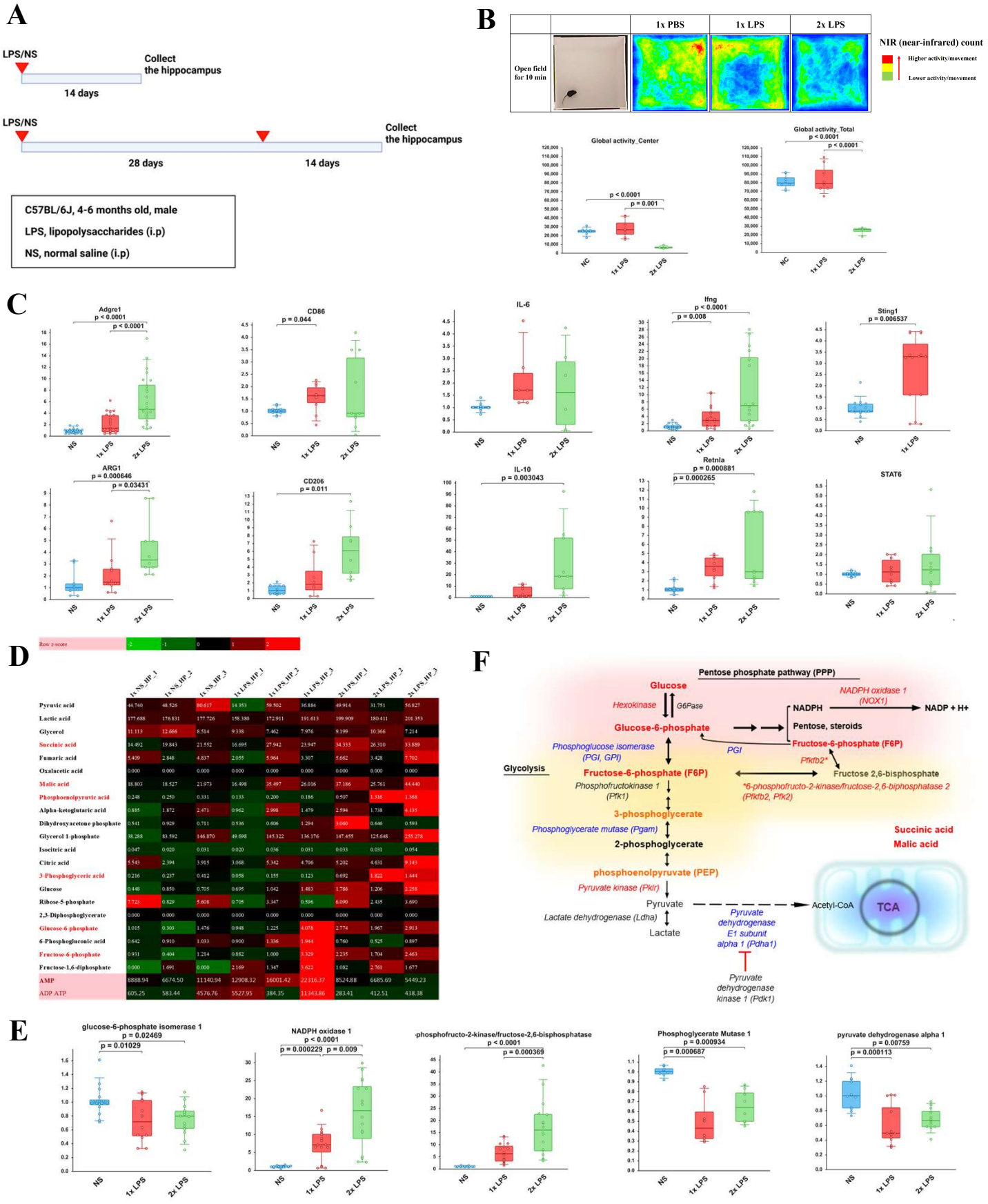

A
LPS/NS
Collect the hippocampus
14 days
LPS/NS
Collect the hippocampus
28 days
14 days
C57BL/6J, 4-6 months old, male
LPS, lipopolysaccharides (i.p)
NS, normal saline (i.p)
B
1x PBS
1x LPS
2x LPS
Open field for 10 min
NIR (near-infrared) count
Higher activity/movement
Lower activity/movement
Global activity_Center
p < 0.0001
p = 0.001
Global activity_Total
p < 0.0001
p < 0.0001
C
Adgre1
p < 0.0001
p < 0.0001
CD86
p = 0.044
IL-6
Ifng
p < 0.0001
p = 0.008
Sting1
p = 0.006537
ARG1
p = 0.000646
p = 0.03431
CD206
p = 0.011
IL-10
p = 0.003043
Retnla
p = 0.000881
p = 0.000265
STAT6
NS
1x LPS
2x LPS
D
Row z-score
1x NS_HP_1
1x NS_HP_2
1x NS_HP_3
1x LPS_HP_1
1x LPS_HP_2
1x LPS_HP_3
2x LPS_HP_1
2x LPS_HP_2
2x LPS_HP_3
Pyruvic acid 44.740 48.526 80.617 14.353 59.502 36.884 49.914 31.751 56.827
Lactic acid 177.688 176.831 177.726 158.380 172.911 191.613 199.909 180.411 201.353
Glycerol 11.113 12.666 8.514 9.338 7.462 7.976 9.199 10.366 7.214
Succinic acid 14.492 19.843 21.552 16.695 27.942 23.947 34.333 26.310 33.889
Fumaric acid 5.409 2.848 4.837 2.055 5.964 3.307 5.662 3.428 7.702
Oxalacetic acid 0.000 0.000 0.000 0.000 0.000 0.000 0.000 0.000 0.000
Malic acid 18.303 18.527 21.973 16.498 35.497 26.016 37.186 25.761 44.440
Phosphoenolpyruvic acid 0.248 0.250 0.331 0.133 0.200 0.186 0.507 1.316 1.368
Alpha-ketoglutaric acid 0.885 1.872 2.471 0.962 2.998 1.479 2.594 1.738 4.335
Dihydroxyacetone phosphate 0.541 0.929 0.711 0.536 0.606 1.294 3.060 0.646 0.593
Glycerol 1-phosphate 38.288 83.592 146.870 49.698 145.322 136.176 147.455 125.648 255.278
Isocitric acid 0.047 0.020 0.031 0.020 0.036 0.031 0.033 0.031 0.054
Citric acid 5.543 2.394 3.915 3.068 5.342 4.706 5.202 4.631 9.143
3-Phosphoglyceric acid 0.216 0.237 0.412 0.058 0.155 0.123 0.692 1.822 1.444
Glucose 0.448 0.850 0.705 0.695 1.042 1.483 1.786 1.206 2.258
Ribose-5-phosphate 7.723 0.829 5.608 0.705 3.347 0.596 6.090 2.435 3.690
2,3-Diphosphoglycerate 0.000 0.000 0.000 0.000 0.000 0.000 0.000 0.000 0.000
Glucose-6-phosphate 1.015 0.303 1.476 0.948 1.225 4.078 2.774 1.967 2.913
6-Phosphogluconic acid 0.642 0.910 1.033 0.900 1.336 1.944 0.760 0.525 0.897
Fructose-6-phosphate 0.931 0.404 1.214 0.882 1.000 3.329 2.255 1.704 2.463
Fructose-1,6-diphosphate 0.000 1.691 0.000 2.169 1.347 3.622 1.082 2.761 1.677
AMP 8888.94 6674.50 11140.94 12908.32 16001.42 22316.37 8524.88 6685.69 5449.23
ADP ATP 605.25 583.44 4576.76 5527.95 384.35 11343.86 283.41 412.51 438.38
F
Pentose phosphate pathway (PPP)
Glucose
Hexokinase
G6Pase
NADPH oxidase 1 (NOX1)
NADPH
NADP + H+
Glucose-6-phosphate
Pentose, steroids
Fructose-6-phosphate (F6P)
PGI
Phosphoglucose isomerase (PGI, GPI)
Pfkfb2*
Glycolysis
Fructose-6-phosphate (F6P)
Fructose 2,6-bisphosphate
Phosphofructokinase 1 (Pfk1)
*6-phosphofructo-2-kinase/fructose-2,6-biphosphatase 2 (Pfkfb2, Pfk2)
3-phosphoglycerate
Phosphoglycerate mutase (Pgam)
Succinic acid
Malic acid
2-phosphoglycerate
phosphoenolpyruvate (PEP)
Pyruvate kinase (Pklr)
Pyruvate
Acetyl-CoA
TCA
Lactate dehydrogenase (Ldha)
Lactate
Pyruvate dehydrogenase E1 subunit alpha 1 (Pdha1)
Pyruvate dehydrogenase kinase 1 (Pdk1)
E
glucose-6-phosphate isomerase
p = 0.02469
p = 0.01029
NADPH oxidase 1
p < 0.0001
p = 0.000229
p = 0.009
-phosphofructo-2-kinase/fructose-2,6-bisphosphatase
p < 0.0001
p = 0.000369
Phosphoglycerate Mutase 1
p = 0.000934
p = 0.000687
pyruvate dehydrogenase alpha 1
p = 0.00759
p = 0.000113
NS
1x LPS
2x LPS

Fig 3

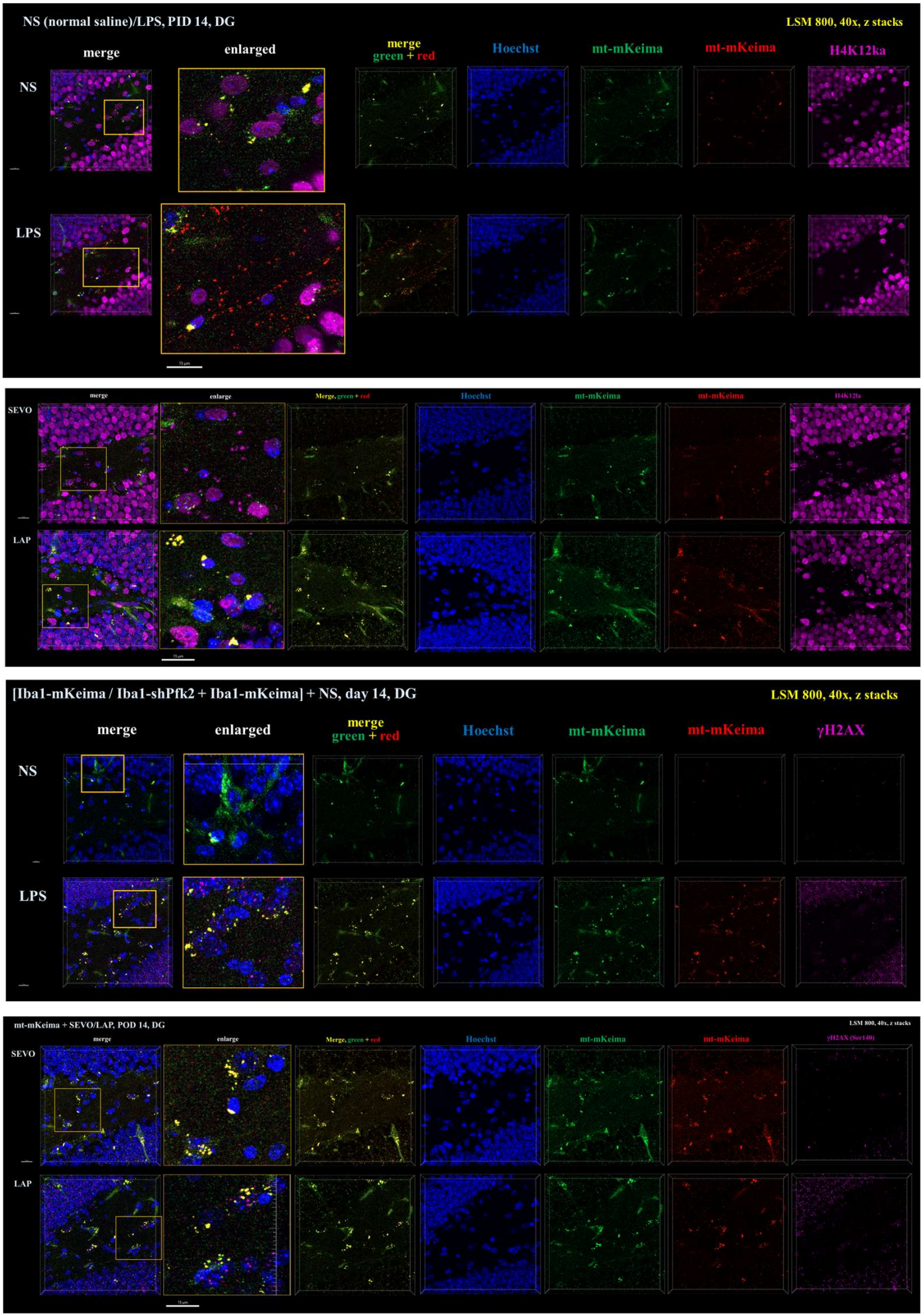

A
NS (normal saline)/LPS, PID 14, DG
LSM 800, 40x, z stacks
merge
enlarged
merge
green + red
Hoechst
mt-mKeima
mt-mKeima
H4K12ka
NS
LPS
B
merge
enlarge
Merge, green + red
Hoechst
mt-mKeima
mt-mKeima
H4K12la
SEVO
LAP
C
[Iba1-mKeima / Iba1-shPfk2 + Iba1-mKeima] + NS, day 14, DG
LSM 800, 40x, z stacks
merge
enlarged
merge
green + red
Hoechst
mt-mKeima
mt-mKeima
γH2AX
NS
LPS
D
mt-mKeima + SEVO/LAP, POD 14, DG
LSM 800, 40x, z stacks
merge
enlarge
Merge, green + red
Hoechst
mt-mKeima
mt-mKeima
γH2AX (Ser140)
SEVO
LAP

Fig 4

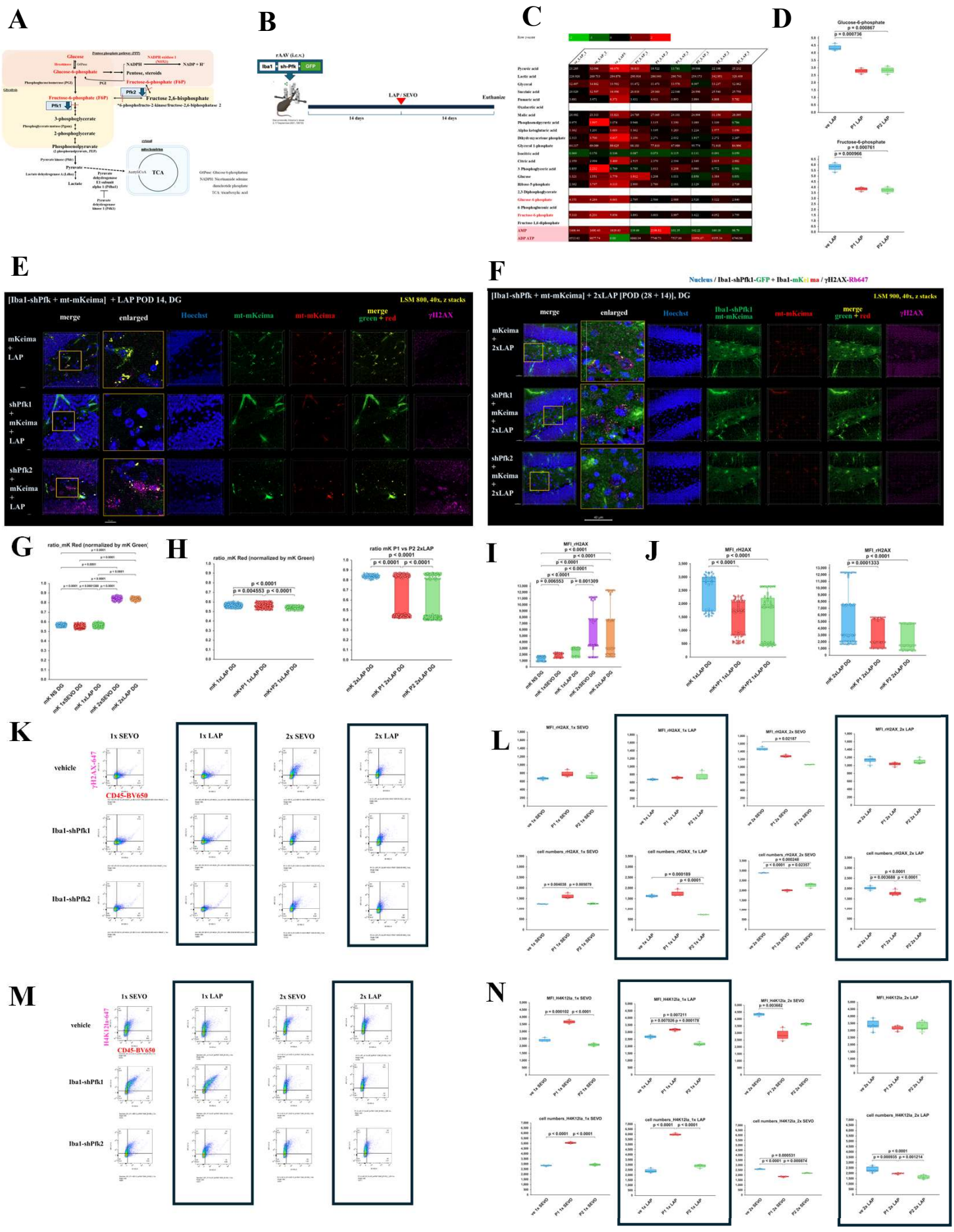

A
B
C
D
E
F
G
H
I
J
K
L
M
N
rAAV (i.c.v.)
Iba1
sh-Pfk
GFP
LAP / SEVO
Euthanize
14 days
14 days
Glucose-6-phosphate
p = 0.000867
p = 0.000736
Fructose-6-phosphate
p = 0.000761
p = 0.000966
[Iba1-shPfk + mt-mKeima] + LAP POD 14, DG
LSM 800, 40x, z stacks
merge
enlarged
Hoechst
mt-mKeima
merge green + red
γH2AX
mKeima + LAP
shPfk1 + mKeima + LAP
shPfk2 + mKeima + LAP
Nucleus / Iba1-shPfk1-GFP + Iba1-mKeima / γH2AX-Rb647
[Iba1-shPfk + mt-mKeima] + 2xLAP [POD (28 + 14)], DG
LSM 900, 40x, z stacks
Iba1-shPfk1 mt-mKeima
mKeima + 2xLAP
shPfk1 + mKeima + 2xLAP
shPfk2 + mKeima + 2xLAP
ratio_mK Red (normalized by mK Green)
ratio mK P1 vs P2 2xLAP
MFI_γH2AX
MFI_γH2AX
MFI_γH2AX
1x SEVO
1x LAP
2x SEVO
2x LAP
vehicle
Iba1-shPfk1
Iba1-shPfk2
γH2AX-647
CD45-BV650
MFI_γH2AX_1x SEVO
MFI_γH2AX_1x LAP
MFI_γH2AX_2x SEVO
MFI_γH2AX_2x LAP
cell numbers_γH2AX_1x SEVO
cell numbers_γH2AX_1x LAP
cell numbers_γH2AX_2x SEVO
cell numbers_γH2AX_2x LAP
H4K12la-647
MFI_H4K12la_1x SEVO
MFI_H4K12la_1x LAP
MFI_H4K12la_2x SEVO
MFI_H4K12la_2x LAP
cell numbers_H4K12la_1x SEVO
cell numbers_H4K12la_1x LAP
cell numbers_H4K12la_2x SEVO
cell numbers_H4K12la_2x LAP

Fig 5

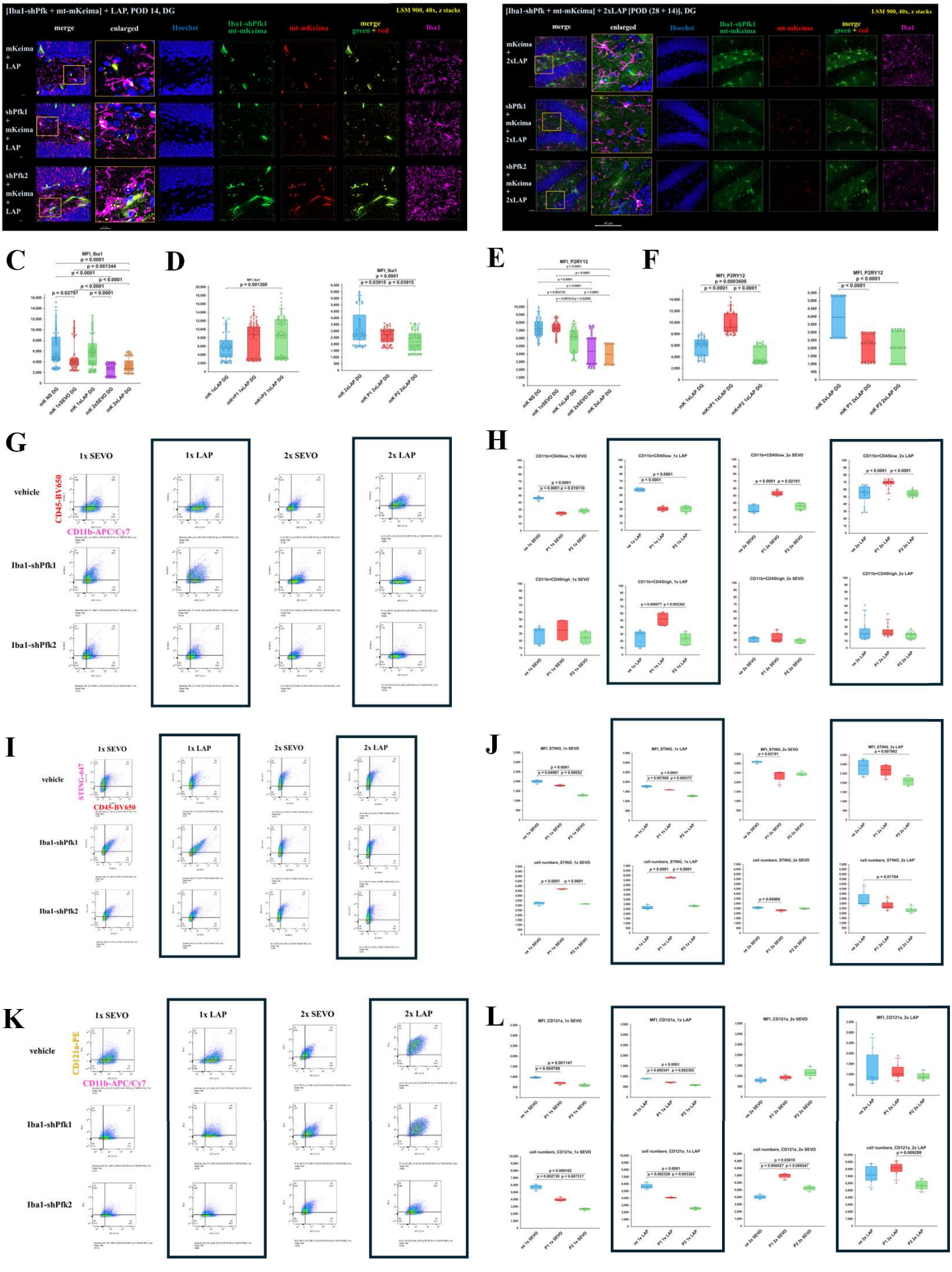

A
[Iba1-shPfk + mt-mKeima] + LAP, POD 14, DG
LSM 900, 40x, z stacks
merge
enlarged
Hoechst
Iba1-shPfk1 mt-mKeima
mt-mKeima
merge green + red
Iba1
mKeima + LAP
shPfk1 + mKeima + LAP
shPfk2 + mKeima + LAP
B
Nucleus / Iba1-shPfk1-GFP + Iba1-mKeima / Iba1-Rb647
[Iba1-shPfk + mt-mKeima] + 2xLAP [POD (28 + 14)], DG
LSM 900, 40x, z stacks
mKeima + 2xLAP
shPfk1 + mKeima + 2xLAP
shPfk2 + mKeima + 2xLAP
C
MFI_Iba1
mK NS DG
mK 1xSEVO DG
mK 1xLAP DG
mK 2xSEVO DG
mK 2xLAP DG
D
MFI_Iba1
mK 1xLAP DG
mK-P1 1xLAP DG
mK-P2 1xLAP DG
MFI_Iba1
mK 2xLAP DG
mK P1 2xLAP DG
mK P2 2xLAP DG
E
MFI_P2RY12
mK NS DG
mK 1xSEVO DG
mK 1xLAP DG
mK 2xSEVO DG
mK 2xLAP DG
F
MFI_P2RY12
mK 1xLAP DG
mK-P1 1xLAP DG
mK-P2 1xLAP DG
MFI_P2RY12
mK 2xLAP DG
mK P1 2xLAP DG
mK P2 2xLAP DG
G
1x SEVO
1x LAP
2x SEVO
2x LAP
vehicle
Iba1-shPfk1
Iba1-shPfk2
CD45-BV650
CD11b-APC/Cy7
H
CD11b+CD45low_1x SEVO
CD11b+CD45low_1x LAP
CD11b+CD45low_2x SEVO
CD11b+CD45low_2x LAP
CD11b+CD45high_1x SEVO
CD11b+CD45high_1x LAP
CD11b+CD45high_2x SEVO
CD11b+CD45high_2x LAP
I
1x SEVO
1x LAP
2x SEVO
2x LAP
vehicle
Iba1-shPfk1
Iba1-shPfk2
STING-647
CD45-BV650
J
MFI_STING_1x SEVO
MFI_STING_1x LAP
MFI_STING_2x SEVO
MFI_STING_2x LAP
cell numbers_STING_1x SEVO
cell numbers_STING_1x LAP
cell numbers_STING_2x SEVO
cell numbers_STING_2x LAP
K
1x SEVO
1x LAP
2x SEVO
2x LAP
vehicle
Iba1-shPfk1
Iba1-shPfk2
CD121a-PE
CD11b-APC/Cy7
L
MFI_CD121a_1x SEVO
MFI_CD121a_1x LAP
MFI_CD121a_2x SEVO
MFI_CD121a_2x LAP
cell numbers_CD121a_1x SEVO
cell numbers_CD121a_1x LAP
cell numbers_CD121a_2x SEVO
cell numbers_CD121a_2x LAP

Fig 6

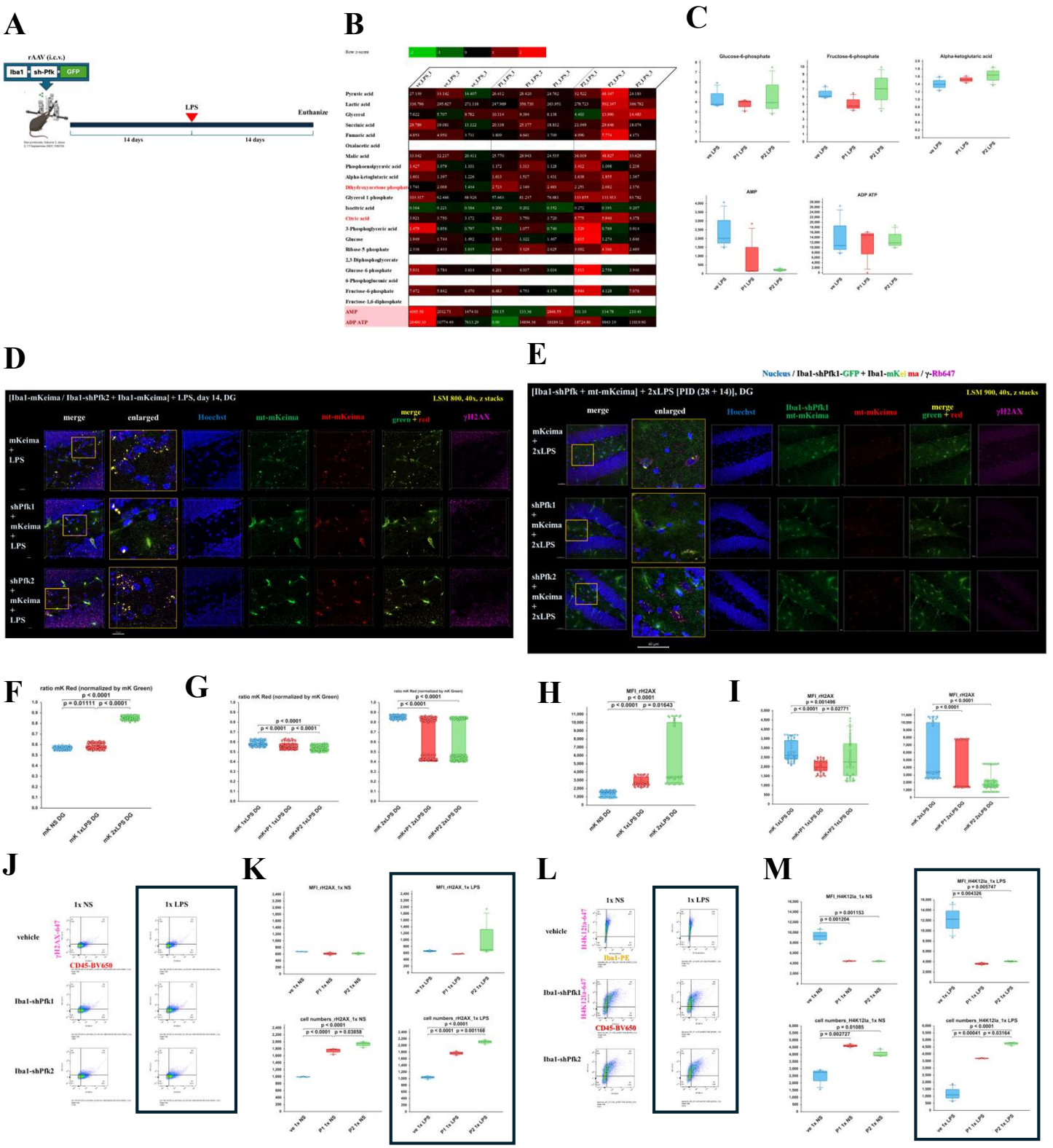

A
rAAV (i.c.v.)
Iba1
sh-Pfk
GFP
LPS
Euthanize
14 days
14 days
B
Row z-score
Pyruvic acid
Lactic acid
Glycerol
Succinic acid
Fumaric acid
Oxalacetic acid
Malic acid
Phosphoenolpyruvic acid
Alpha-ketoglutaric acid
Dihydroxyacetone phosphate
Glycerol 1-phosphate
Isocitric acid
Citric acid
3-Phosphoglyceric acid
Glucose
Ribose-5-phosphate
2,3-Diphosphoglycerate
Glucose-6-phosphate
6-Phosphogluconic acid
Fructose-6-phosphate
Fructose-1,6-diphosphate
AMP
ADP ATP
C
Glucose-6-phosphate
Fructose-6-phosphate
Alpha-ketoglutaric acid
AMP
ADP ATP
D
[Iba1-mKeima / Iba1-shPfk2 + Iba1-mKeima] + LPS, day 14, DG
LSM 800, 40x, z stacks
merge
enlarged
Hoechst
mt-mKeima
mt-mKeima
merge green + red
γH2AX
mKeima + LPS
shPfk1 + mKeima + LPS
shPfk2 + mKeima + LPS
E
Nucleus / Iba1-shPfk1-GFP + Iba1-mKeima / γ-Rb647
[Iba1-shPfk + mt-mKeima] + 2xLPS [PID (28 + 14)], DG
LSM 900, 40x, z stacks
merge
enlarged
Hoechst
Iba1-shPfk1 mt-mKeima
mt-mKeima
merge green + red
γH2AX
mKeima + 2xLPS
shPfk1 + mKeima + 2xLPS
shPfk2 + mKeima + 2xLPS
F
ratio mK Red (normalized by mK Green)
p < 0.0001
p = 0.01111
p < 0.0001
mK NS DG
mK 1xLPS DG
mK 2xLPS DG
G
ratio mK Red (normalized by mK Green)
p < 0.0001
p < 0.0001
p < 0.0001
mK 1xLPS DG
mK-P1 1xLPS DG
mK-P2 1xLPS DG
p < 0.0001
p < 0.0001
mK 2xLPS DG
mK-P1 2xLPS DG
mK-P2 2xLPS DG
H
MFI_rH2AX
p < 0.0001
p < 0.0001
p = 0.01643
mK NS DG
mK 1xLPS DG
mK 2xLPS DG
I
MFI_rH2AX
p = 0.001496
p < 0.0001
p = 0.02771
mK 1xLPS DG
mK-P1 1xLPS DG
mK-P2 1xLPS DG
MFI_rH2AX
p < 0.0001
p < 0.0001
mK 2xLPS DG
mK P1 2xLPS DG
mK P2 2xLPS DG
J
1x NS
1x LPS
vehicle
Iba1-shPfk1
Iba1-shPfk2
γH2AX-647
CD45-BV650
K
MFI_rH2AX_1x NS
MFI_rH2AX_1x LPS
cell numbers_rH2AX_1x NS
p < 0.0001
p < 0.0001
p = 0.03858
cell numbers_rH2AX_1x LPS
p < 0.0001
p < 0.0001
p = 0.001168
L
1x NS
1x LPS
vehicle
Iba1-shPfk1
Iba1-shPfk2
H4K12la-647
Iba1-PE
CD45-BV650
M
MFI_H4K12la_1x NS
p = 0.001153
p = 0.001204
cell numbers_H4K12la_1x NS
p = 0.001085
p = 0.002727
MFI_H4K12la_1x LPS
p = 0.005747
p = 0.004326
cell numbers_H4K12la_1x LPS
p < 0.0001
p = 0.00041
p = 0.03164

Fig 7

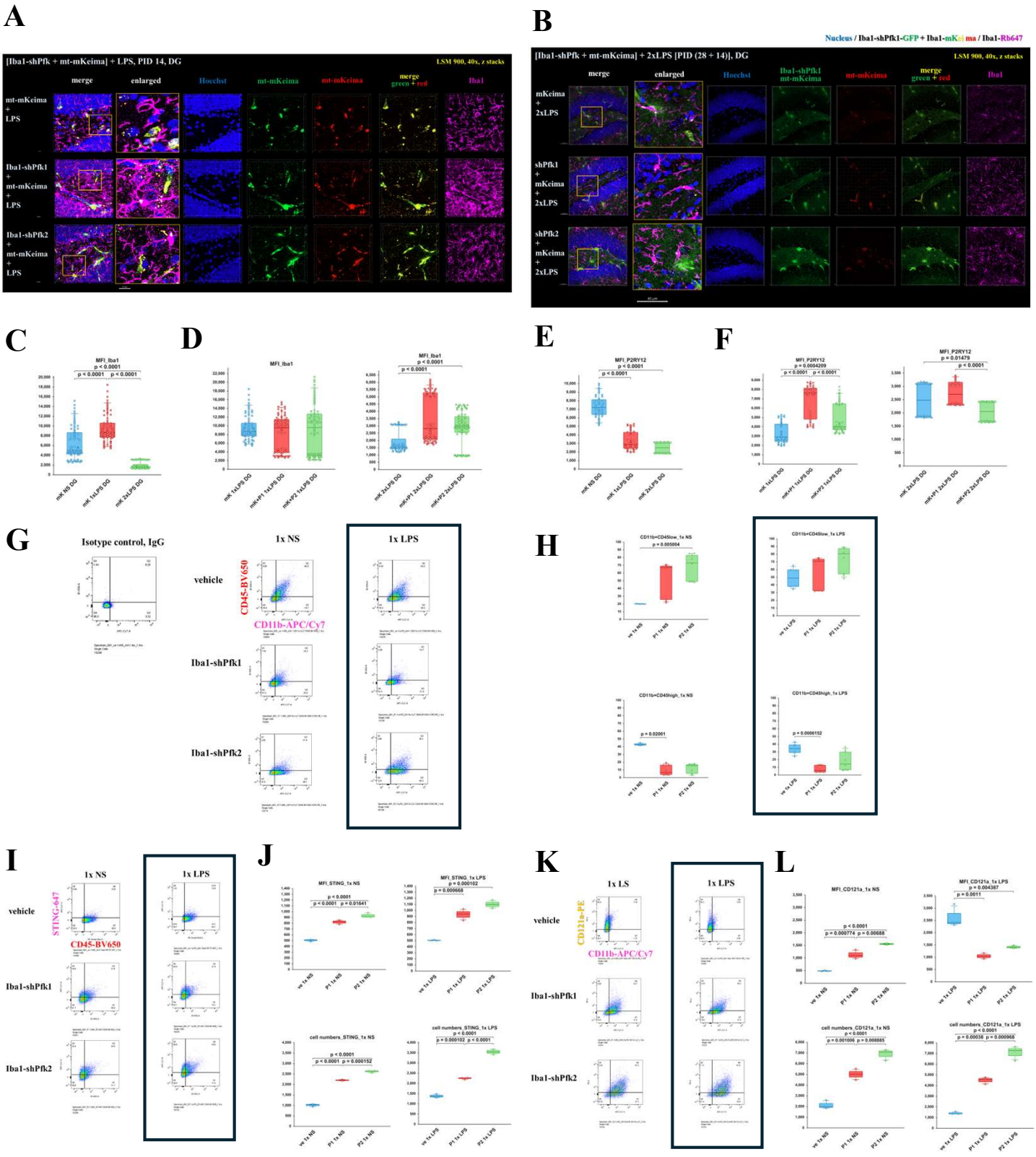
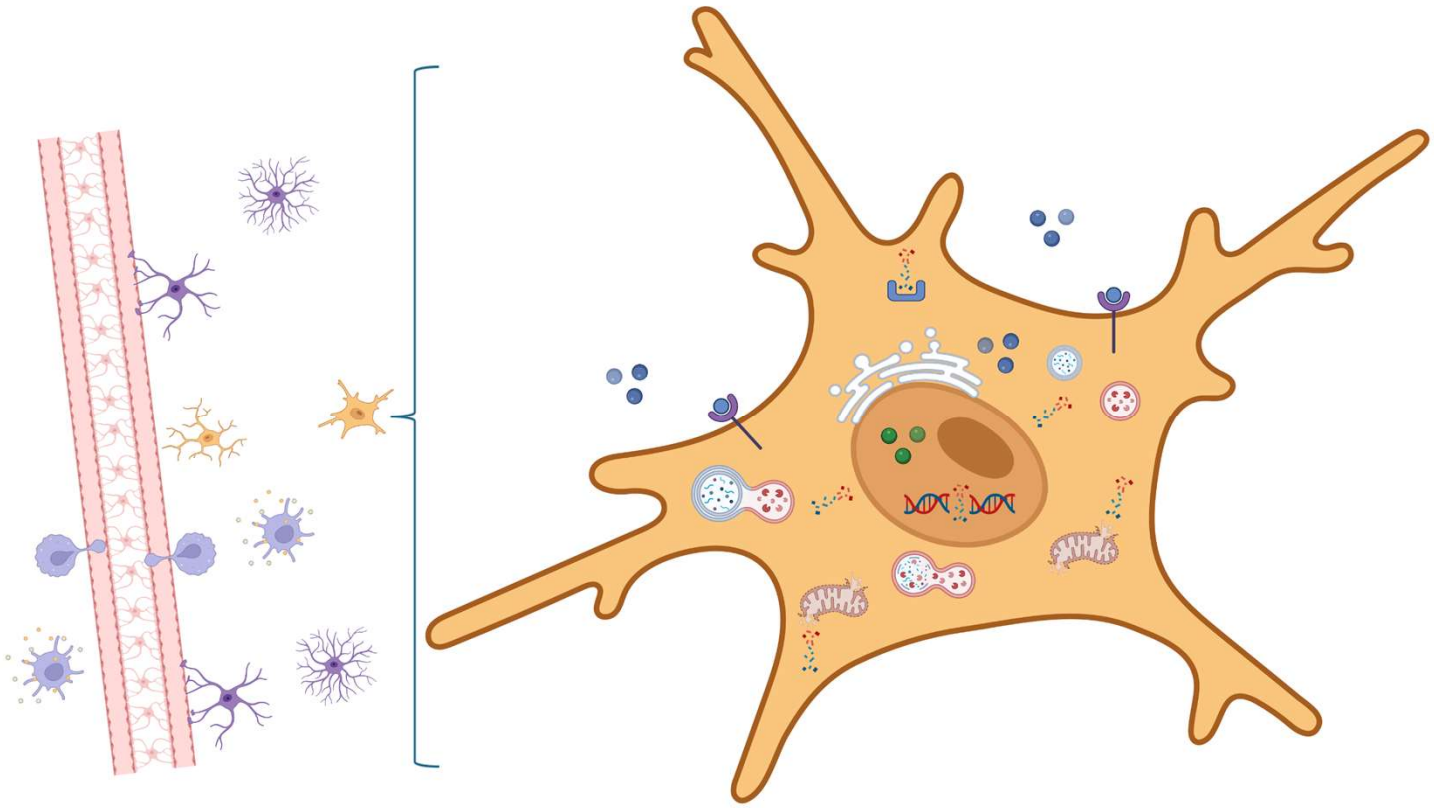

A
[Iba1-shPfk + mt-mKeima] + LPS, PID 14, DG
LSM 900, 40x, z stacks
merge
enlarged
Hoechst
mt-mKeima
mt-mKeima
merge green + red
Iba1
mt-mKeima + LPS
Iba1-shPfk1 + mt-mKeima + LPS
Iba1-shPfk2 + mt-mKeima + LPS
B
Nucleus / Iba1-shPfk1-GFP + Iba1-mKeima / Iba1-Rb647
[Iba1-shPfk + mt-mKeima] + 2xLPS [PID (28 + 14)], DG
LSM 900, 40x, z stacks
merge
enlarged
Hoechst
Iba1-shPfk1 mt-mKeima
mt-mKeima
merge green + red
Iba1
mKeima + 2xLPS
shPfk1 + mKeima + 2xLPS
shPfk2 + mKeima + 2xLPS
C
MFI_Iba1
p < 0.0001
p < 0.0001 p < 0.0001
mK NS DG
mK 1xLPS DG
mK 2xLPS DG
D
MFI_Iba1
mK 1xLPS DG
mK-P1 1xLPS DG
mK-P2 1xLPS DG
MFI_Iba1
p < 0.0001
p < 0.0001
mK 2xLPS DG
mK-P1 2xLPS DG
mK-P2 2xLPS DG
E
MFI_P2RY12
p < 0.0001
p < 0.0001
mK NS DG
mK 1xLPS DG
mK 2xLPS DG
F
MFI_P2RY12
p = 0.0004209
p < 0.0001 p < 0.0001
mK 1xLPS DG
mK-P1 1xLPS DG
mK-P2 1xLPS DG
MFI_P2RY12
p = 0.01479
p < 0.0001
mK 2xLPS DG
mK-P1 2xLPS DG
mK-P2 2xLPS DG
G
Isotype control, IgG
1x NS
1x LPS
vehicle
Iba1-shPfk1
Iba1-shPfk2
CD45-BV650
CD11b-APC/Cy7
H
CD11b+CD45low_1x NS
p = 0.005004
ve 1x NS
P1 1x NS
P2 1x NS
CD11b+CD45low_1x LPS
ve 1x LPS
P1 1x LPS
P2 1x LPS
CD11b+CD45high_1x NS
p = 0.02001
CD11b+CD45high_1x LPS
p = 0.0006152
I
1x NS
1x LPS
vehicle
Iba1-shPfk1
Iba1-shPfk2
STING-647
CD45-BV650
J
MFI_STING_1x NS
p < 0.0001
p < 0.0001 p = 0.01641
MFI_STING_1x LPS
p = 0.000102
p = 0.000668
cell numbers_STING_1x NS
p < 0.0001
p < 0.0001 p = 0.000152
cell numbers_STING_1x LPS
p < 0.0001
p = 0.000102 p < 0.0001
K
1x LS
1x LPS
vehicle
Iba1-shPfk1
Iba1-shPfk2
CD121a-PE
CD11b-APC/Cy7
L
MFI_CD121a_1x NS
p < 0.0001
p = 0.000774 p = 0.00688
MFI_CD121a_1x LPS
p = 0.004387
p = 0.0011
cell numbers_CD121a_1x NS
p < 0.0001
p = 0.001006 p = 0.008885
cell numbers_CD121a_1x LPS
p < 0.0001
p = 0.00038 p = 0.000968

Fig 8





Inflamed microglia



Damaged mitochondria



Damaged double strand DNA



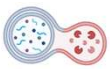
Fragmented double strand DNA



Autophagosome



Lysosome



Autolysosome



cGAS



precursor form of IL-1



IL-1



IL-1R, CD121a

Supplementary Files

This is a list of supplementary files associated with this preprint. Click to download.

- SupplementaryfiguresCMIKateInyoungOHTheUniversityofHongKong.pdf
- RawimagesFig5.KCMI2026KateInyoungOHTheUniversityofHongKong.pptx
- RawimagesFig6.JCMI2026KateInyoungOHTheUniversityofHongKong.pptx
- RawimagesFig2.B.iCMI2026KateInyoungOHTheUniversityofHongKong.pptx
- RawimagesFig7.GCMI2026KateInyoungOHTheUniversityofHongKong.pptx
- RawimagesFig4.KCMI2026KateInyoungOHTheUniversityofHongKong.pptx
- RawimagesFig7.ICMI2026KateInyoungOHTheUniversityofHongKong.pptx
- RawimagesFig4.MCMI2026KateInyoungOHTheUniversityofHongKong.pptx
- RawimagesFig7.KCMI2026KateInyoungOHTheUniversityofHongKong.pptx
- RawimagesFig1.B.iCMI2026KateInyoungOHTheUniversityofHongKong.pptx
- RawimagesSupplementaryFigS2.GKateInyoungOHTheUniversityofHongKong.pptx
- RawimagesSupplementaryFigS2.EKateInyoungOHTheUniversityofHongKong.pptx
- RawimagesSupplementaryFigS2.C.iKateInyoungOHTheUniversityofHongKong.pptx
- RawimagesFig6.ECMI2026KateInyoungOHTheUniversityofHongKong.pptx
- RawimagesSupplementaryFigS2.C.iiKateInyoungOHTheUniversityofHongKong.pptx
- RawimagesFig4.FCMI2026KateInyoungOHTheUniversityofHongKong.pptx
- RawimagesFig5.BCMI2026KateInyoungOHTheUniversityofHongKong.pptx
- SupplementaryfiguresCMI2026KateInyoungOHTheUniversityofHongKong.pptx
- RawimagesFig3.CCMI2026KateInyoungOHTheUniversityofHongKong.pptx
- RawimagesFig3.ACMI2026KateInyoungOHTheUniversityofHongKong.pptx
- RawimagesFig3.DCMI2026KateInyoungOHTheUniversityofHongKong.pptx
- RawimagesSupplementaryFigS1.AKateInyoungOHTheUniversitofHongKong.pptx
- RawimagesFig3.BCMI2026KateInyoungOHTheUniversityofHongKong.pptx
- RawimagesFig4.ECMI2026KateInyoungOHTheUniversityofHongKong.pptx
- RawimagesFig5.ACMI2026KateInyoungOHTheUniversityofHongKong.pptx
- RawimagesFig7.ACMI2026KateInyoungOHTheUniversityofHongKong.pptx
- RawimagesSupplementaryFigS2.DKateInyoungOHTheUniversityofHongKong.pptx
- RawimagesFig6.DCMI2026KateInyoungOHTheUniversityofHongKong.pptx
- RawimagesFig5.GCMI2026KateInyoungOHTheUniversityofHongKong.pptx
- RawimagesSupplementaryFigS2.AKateInyoungOHTheUniversityofHongKong.pptx
- RawimagesFig7.BCMI2026KateInyoungOHTheUniversityofHongKong.pptx
- RawimagesSupplementaryFigS1.BKateInyoungOHTheUniversityofHongKong.pptx

- RawimagesSupplementaryFigS2.BKateInyoungOHTheUniversityofHongKong.pptx
- RawimagesSupplementaryFigS1.DKateInyoungOHTheUniversityofHongKong.pptx
- RawimagesSupplementaryFigS1.CKateInyoungOHTheUniversityofHongKong.pptx
- RawimagesFig5.ICMI2026KateInyoungOHTheUniversityofHongKong.pptx
- RawimagesFig6.LCMI2026KateInyoungOHTheUniversityofHongKong.pptx
- CombinedwithmarkingRawimagesSupplementryFiguresKateInyoungOHTheUniversityofHongKong.pdf
- CombinedwithmarkingRawimagesFiguresKateInyoungOHTheUniversityofHongKong.pdf
- CombinedwithmarkingRawSupplementryFiguresKateInyoungOHTheUniversityofHK.pptx
- CombinedwithmarkingRawimagesFiguresKateInyoungOHTheUniversityofHongKong.pptx